WILEY

A mathematical model that integrates cardiac electrophysiology, mechanics, and fluid dynamics: Application to the human left heart

Michele Bucelli[1] ⓘ　|　**Alberto Zingaro**[1] ⓘ　|　**Pasquale Claudio Africa**[1] ⓘ　|　**Ivan Fumagalli**[1] ⓘ　|　**Luca Dede'**[1] ⓘ　|　**Alfio Quarteroni**[1,2] ⓘ

[1]MOX, Dipartimento di Matematica, Politecnico di Milano, Milan, Italy

[2]Institute of Mathematics, École Polytechnique Fédérale de Lausanne, Lausanne, Switzerland

Correspondence
Michele Bucelli, MOX, Dipartimento di Matematica Politecnico di Milano, P.zza Leonardo da Vinci 32, 20133 Milan, Italy.
Email: michele.bucelli@polimi.it

Abstract

We propose a mathematical and numerical model for the simulation of the heart function that couples cardiac electrophysiology, active and passive mechanics and hemodynamics, and includes reduced models for cardiac valves and the circulatory system. Our model accounts for the major feedback effects among the different processes that characterize the heart function, including electro-mechanical and mechano-electrical feedback as well as force-strain and force-velocity relationships. Moreover, it provides a three-dimensional representation of both the cardiac muscle and the hemodynamics, coupled in a fluid–structure interaction (FSI) model. By leveraging the multiphysics nature of the problem, we discretize it in time with a segregated electrophysiology-force generation-FSI approach, allowing for efficiency and flexibility in the numerical solution. We employ a monolithic approach for the numerical discretization of the FSI problem. We use finite elements for the spatial discretization of partial differential equations. We carry out a numerical simulation on a realistic human left heart model, obtaining results that are qualitatively and quantitatively in agreement with physiological ranges and medical images.

KEYWORDS
blood circulation, cardiac modeling, electromechanics, fluid–structure interaction, multiphysics modeling

1 | INTRODUCTION

Cardiovascular diseases represent the major cause of death in the adult population of the western world.[1] While in-vivo measuring techniques allow to inspect and quantify the heart function and dysfunction, these measures often lack resolution or accuracy, and may be invasive. Mathematical models for computational medicine can provide tools to simulate the human heart function, complementing experimental measurements, providing further insight into the cardiac function, and assisting in the development of personalized treatments.[2–7]

The heart function results from the interplay of several different physical processes,[8,9] ranging from the sub-cellular scale to the tissue one. Electrochemical processes drive the excitation of cardiac muscular cells, resulting in the generation of an active force during contraction that, together with the passive mechanical properties of the cardiac tissue, interacts with the blood within the heart chambers, pumping it towards the circulatory system. Understanding and then modeling the multiphysics and multiscale nature of the heart function, as well as feedback effects among its components, is crucial for constructing an accurate computational model of the heart.[6,10–12]

Several mathematical and numerical heart models have been proposed in recent years. Most of them focus on some specific feature of the heart function, by surrogating the remaining ones with models of reduced dimensionality: electrophysiology,[13–20] cardiac mechanics and electromechanics[2,21–33] or computational fluid dynamics (CFD) of the blood.[4,34–43] Only few works also consider the interplay between hemodynamics and cardiac mechanics in a fluid–structure interaction (FSI) framework,[44–48] while neglecting or simplifying the electrical processes generating the contraction.[49–52]

Albeit each of the above-mentioned models can provide meaningful insight into the cardiac function in both healthy and pathological conditions, they often neglect the feedback mechanisms that relate the different components. Conversely, fully integrated models featuring multiphysics coupling of electrophysiology, mechanics and fluid dynamics[12,53–56] can provide a very accurate description of the physics of the heart, at the price of a high model complexity and large computational cost.

One of the first fully coupled heart models was provided by the UT-Heart simulator,[10,11,55] and was subsequently employed for personalized clinical case studies.[57] Another fully coupled model was proposed in Reference [12]. There, the authors focus on right and left ventricular systole, while providing a simplified description of the atria and neglecting the presence of valves, at the same time providing important details on the computational strategies that allow to exploit high-performance computing facilities for cardiac simulations. In Reference [58], a biventricular fully coupled model is proposed for the study of a left ventricular assist device. The complexity of the model is leveraged to analyze the effect of different working regimes of the device, both on the hemodynamics and on the mechanical function of the heart. In Reference [59,60], a coupled fluid–structure-electrophysiology left heart model is presented, relying on the immersed boundary method in a finite volumes /finite differences combined framework for the numerical discretization. The model yields a good agreement with physiology, in terms of both mechanical and hemodynamic indicators. However, it uses a simplified phenomenological description of force generation,[61] neglecting feedbacks from fiber shortening; moreover, the interplay between heart and circulation is treated by means of Windkessel models. The same authors also provide a GPU-accelerated version of the same model in Reference [62], obtaining a significant computational speedup, and they extend the model to a whole heart in Reference [63], at the same time presenting a proof-of-concept virtual clinical trial that highlights how fully coupled models of this type can have a significant impact on the clinical practice. Finally, in Reference [64] a simplified 2D fluid–structure-electrophysiology interaction model is developed for embryonic hearts. To the best of our knowledge, no other works focus on a fully integrated model of the heart.

In this work, we propose a novel multiphysics coupled model featuring a three-dimensional description of cardiac electrophysiology, active and passive mechanics, and hemodynamics, together with a closed-loop lumped-parameter model to simulate systemic and pulmonary circulation. We will refer to the different physical components (electrophysiology, contractile force generation, mechanics, fluid dynamics, circulation) as *core models*. The proposed model includes several of the feedback mechanisms that regulate the heart function, including mechano-electric feedbacks,[65] force-strain and force-velocity relationships,[66] FSI between the blood and the muscle,[67] and the feedback between the heart and the circulation.[30,43,68] In particular, the feedback between force generation and fiber shortening and shortening velocity was found to be highly important in cardiac electromechanics,[24] allowing to obtain physiologically realistic flow rates through semilunar valves that would otherwise be significantly higher than what is experimentally observed. The force-strain relationship, instead, is the microscopic basis for the macroscopic Frank-Starling effect. Moreover, FSI modeling allows to capture dynamic effects such as the presence of pressure gradients and pressure waves, overcoming some of the limitations of uncoupled CFD and electromechanics models, such as the inability of the former to reproduce isovolumetric phases.[40,69] We test our model on a realistic human left heart, comprising the left ventricle, left atrium and a portion of the ascending aorta, as well as the mitral and aortic valves.

Due to the complexity and large scale of the problem at hand, it is crucial to employ efficient numerical schemes for its solution. A critical issue is the numerical treatment of the coupling conditions between the different core models. One possible approach is to solve the fully coupled problem monolithically.[54] However, this requires the development of complex solvers and ad-hoc preconditioners, and it lacks flexibility in the choice of the discretization schemes and parameters for each core model. Inspired by Reference [30], we choose a segregated-staggered scheme, in which all coupling terms are treated explicitly when possible. Implicit, monolithic coupling is used for fluid–structure interaction.[67] Spatial

discretization is achieved by means of the finite element method.[70,71] The proposed computational framework leverages high-performance computing techniques to enable large-scale simulations, based on the finite element library life.[72–74]

We run a numerical simulation and compare the value of several indicators against normal ranges, obtaining a satisfactory agreement. A qualitative match with physiological behavior is also observed in terms of ventricular pressure and volume traces, as well as three dimensional deformation and flow patterns. Overall, the results indicate that the proposed computational framework can provide an accurate and physiologically sound description of the physics of the heart.

This paper is structured as follows: in Section 2, we present in detail the mathematical models employed and the numerical scheme. Section 3 presents and analyzes the simulation results. Finally, in Section 4, we point at some shortcomings in the proposed model, and, in Section 5, we draw some conclusive remarks.

2 | MODELS AND METHODS

In the following sections, we provide details on the mathematical models used in the description of the heart and on the numerical methods used in their discretization.

2.1 | Mathematical models

Let $\Omega \subset \mathbb{R}^3$ be an open, bounded domain, changing in time and representing the volume occupied by a human left heart at every time instant during the heartbeat. We partition the domain into the subdomains Ω_f and Ω_s (see Figure 1), representing the volume occupied by the blood and that occupied by the solid heart wall respectively. We denote their interface by $\Sigma = \partial\Omega_f \cap \partial\Omega_s$. We further partition the fluid and solid subdomains into Ω_i^{LV}, Ω_i^{LA}, Ω_i^{AA} and Ω_i^{ring}, for $i \in \{f, s\}$, representing the left ventricle (LV), the left atrium (LA), the ascending aorta (AA) and the valve region (including both the mitral and the aortic valve, Section 2.1.4), for either the fluid or the solid domains. On the boundary of any of the defined sets, $\mathbf{n}$ denotes the outward directed normal unit vector. On Σ, $\mathbf{n}$ denotes the normal unit vector directed outward from the fluid domain and inward into the solid domain.

All the previously defined domains are moving in time as the heart beats (to keep the notation light, we omit the explicit dependence of the domains on time). We define a fixed *reference configuration* $\widehat{\Omega}$ to keep track of the deformation. For each of the previously defined sets, we use a hat to denote the corresponding set in reference configuration. We refer to the moving configuration as the *current configuration*. The evolution in time of the current configuration is described by the following maps:
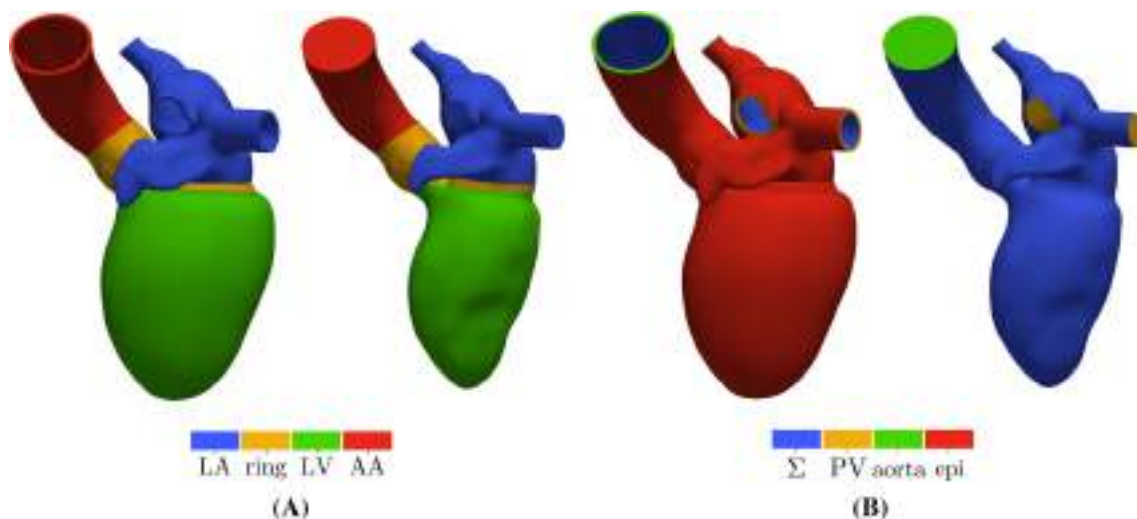
FIGURE 1 Solid (A,B, on the left) and fluid (A,B, on the right) computational domains. (A) Partition of the domain volume into Ω_i^{LV} (left ventricle), Ω_i^{LA} (left atrium), Ω_i^{AA} (ascending aorta) and Ω_i^{ring} (mitral and aortic valve regions), where the subscript $i \in \{s, f\}$ denotes the fluid and solid subdomains, respectively. (B) Partition of the boundary into walls, inlets and outlet sections and fluid–solid interface

$$\mathscr{L}_s : \widehat{\Omega}_s(0, T) \to \Omega_s \qquad \Omega_s = \left\{ \mathbf{x} = \mathscr{L}_s(\widehat{\mathbf{x}}, \ t) \ , \widehat{\mathbf{x}} \in \widehat{\Omega}_s \right\},$$

$$\mathscr{L}_f : \widehat{\Omega}_f(0, T) \to \Omega_f \qquad \Omega_f = \left\{ \mathbf{x} = \mathscr{L}_f(\widehat{\mathbf{x}}, \ t) \ , \widehat{\mathbf{x}} \in \widehat{\Omega}_f \right\}.$$

The precise definition of the maps depends on the physical models defined on each subdomain, and is detailed in the following sections.

We denote by $t \in (0, T)$ the independent variable representing time, by $\mathbf{x}$ the spatial coordinates in the current configuration, and by $\widehat{\mathbf{x}}$ the spatial coordinates in reference configuration.

We consider a coupled problem involving several physical models: electrophysiology, active force generation, cardiac FSI and circulation hemodynamics. The unknowns of the model are determined by solving a coupled system of differential equations representing an electrophysiology-mechanics-fluid dynamics (EMF) interaction problem:

$$
\begin{aligned}
v &: \widehat{\Omega}_s^{LV} \times (0, T) \to \mathbb{R} && \text{transmembrane potential,} \\
\mathbf{w} &: \widehat{\Omega}_s^{LV} \times (0, T) \to \mathbb{R}^{N_{ion}^w} && \text{ionic gating variables,} \\
\mathbf{z} &: \widehat{\Omega}_s^{LV} \times (0, T) \to \mathbb{R}^{N_{ion}^z} && \text{ionic concentrations,} \\
\mathbf{s} &: \widehat{\Omega}_s^{LV} \times (0, T) \to \mathbb{R}^{N_{act}} && \text{activation state,} \\
\mathbf{d} &: \widehat{\Omega}_s \times (0, T) \to \mathbb{R}^3 && \text{solid displacement,} \\
\mathbf{d}_{ALE} &: \widehat{\Omega}_f \times (0, T) \to \mathbb{R}^3 && \text{fluid domain displacement,} \\
\mathbf{u} &: \Omega_f \times (0, T) \to \mathbb{R}^3 && \text{fluid velocity,} \\
p &: \Omega_f \times (0, T) \to \mathbb{R} && \text{pressure,} \\
\mathbf{c} &: (0, T) \to \mathbb{R}^{N_{circ}} && \text{circulation state variables.}
\end{aligned}
$$

The remainder of this section is devoted to the description of the models and equations that compose the EMF problem. In the following, we omit the numerical values of all the parameters mentioned, that could be found in Appendix D.

2.1.1 | Fiber generation

Cardiac tissue is organized in sheets of fibers, which determine a preferential direction for the conduction of the electrical signal,[8,9,75] and are relevant in characterizing the passive and active mechanical properties of the cardiac muscle.[76,77] We incorporate fibers in the model by defining, at every point $\widehat{\mathbf{x}} \in \widehat{\Omega}_s$, a local orthonormal basis $\{\mathbf{f}_0, \mathbf{s}_0, \mathbf{n}_0\}$ representing the local direction of fibers, fiber sheets and normal to fiber sheets.[17]

As the fiber direction is rarely available from experimental data, it is often reconstructed in a preprocessing step using rule-based algorithms.[17,78,79] For our left heart model, we combine different Laplace-Dirichlet Rule-Based Methods (LDRBMs), namely the one presented in Reference [80] for ventricular fibers and the one presented in Reference [17] for left atrial fibers.

2.1.2 | Electrophysiology

Cardiac cells can be excited by an electrical stimulus, triggering a series of subcellular mechanisms resulting in an *action potential* that manifests as a variation in time of the *transmembrane potential*,[8,9,81,82] that is, the difference of potential between the intracellular and extracellular spaces.

We model the ventricle $\widehat{\Omega}_s^{LV}$ as electrically excitable, while other portions of the solid domain, including $\widehat{\Omega}_s^{LA}$, are regarded as electrically passive, i.e. they do not generate action potentials. We remark that this is a simplification for what concerns the LA (see Section 4).

The evolution of the transmembrane potential v is described by the monodomain equation[81] augmented with the mechano-electric feedbacks.[65] Let $F = I + \mathbf{d}$ and $J = \det F$. The monodomain equation reads

$$
\begin{cases}
J\chi C_{\mathrm{m}}\dfrac{\partial v}{\partial t} - \nabla \cdot \left(JF^{-1}D_{\mathrm{m}}F^{-T}\nabla v\right) + J\chi I_{\mathrm{ion}}(v,\ \mathbf{w},\ \mathbf{z}) = J\chi I_{\mathrm{app}}(\widehat{\mathbf{x}},\ t) & \text{in } \widehat{\Omega}_{\mathrm{s}}^{\mathrm{LV}} \times (0,\ T)\,, \\[2mm]
JF^{-1}D_{\mathrm{m}}F^{-T}\nabla v \cdot \widehat{\mathbf{n}} = 0 & \text{on } \partial\widehat{\Omega}_{\mathrm{s}}^{\mathrm{LV}} \times (0,\ T)\,, \\[2mm]
v = v_0 & \text{in } \widehat{\Omega}_{\mathrm{s}}^{\mathrm{LV}} \times \{0\}\,,
\end{cases}
\tag{1}
$$

where χ and C_{m} are the membrane surface-to-volume ratio and membrane capacitance, respectively.

The vector $\mathbf{w}$ collects the recovery (or gating) variables,[81] that for a single cell represent fractions of open ionic channels, while $\mathbf{z}$ is a vector of ionic concentrations. Most notably, one of the variables within the vector $\mathbf{z}$ represents the intracellular calcium concentration $\left[\mathrm{Ca}^{2+}\right]_{\mathrm{i}}$. The evolution of $\mathbf{w}$ and $\mathbf{z}$ is modeled by coupling (1) with the ionic model by ten Tusscher and Panfilov,[83] which also defines the ionic current $I_{\mathrm{ion}}(v, \mathbf{w}, \mathbf{z})$. The model is expressed by a system of ODEs defined at each point $\widehat{\mathbf{x}} \in \widehat{\Omega}_{\mathrm{s}}^{\mathrm{LV}}$:

$$
\begin{cases}
\dfrac{\partial \mathbf{w}}{\partial t} = \mathbf{F}_{\mathrm{ion}}^{\mathbf{w}}(v,\ \mathbf{w}) & \text{in } \widehat{\Omega}_{\mathrm{s}}^{\mathrm{LV}} \times (0,\ T)\,, \\[2mm]
\dfrac{\partial \mathbf{z}}{\partial t} = \mathbf{F}_{\mathrm{ion}}^{\mathbf{z}}(v,\ \mathbf{w},\ \mathbf{z}) & \text{in } \widehat{\Omega}_{\mathrm{s}}^{\mathrm{LV}} \times (0,\ T)\,, \\[2mm]
\mathbf{w} = \mathbf{w}_0 & \text{in } \widehat{\Omega}_{\mathrm{s}}^{\mathrm{LV}} \times \{0\}\,, \\[2mm]
\mathbf{z} = \mathbf{z}_0 & \text{in } \widehat{\Omega}_{\mathrm{s}}^{\mathrm{LV}} \times \{0\}\,.
\end{cases}
$$

We remark that $\mathbf{F}_{\mathrm{ion}}^{\mathbf{w}}$ and $\mathbf{F}_{\mathrm{ion}}^{\mathbf{z}}$ do not involve spatial derivatives of $\mathbf{w}$, $\mathbf{z}$ or v. For the precise definition of $\mathbf{F}_{\mathrm{ion}}^{\mathbf{w}}$, $\mathbf{F}_{\mathrm{ion}}^{\mathbf{z}}$ and I_{ion}, we refer to Reference [83]. The initial states v_0, $\mathbf{w}_0$ and $\mathbf{z}_0$ are obtained by solving a reduced, zero-dimensional monodomain equation for a large number of heartbeats, until a periodic limit cycle is reached.[30,81]

The tensor D_{m} in (1) incorporates the conductivity properties of the tissue, and is defined as

$$
D_{\mathrm{m}} = \sigma_{\mathrm{m}}^{\mathrm{l}}\frac{F\mathbf{f}_0 \otimes F\mathbf{f}_0}{\|F\mathbf{f}_0\|^2} + \sigma_{\mathrm{m}}^{\mathrm{t}}\frac{F\mathbf{s}_0 \otimes F\mathbf{s}_0}{\|F\mathbf{s}_0\|^2} + \sigma_{\mathrm{m}}^{\mathrm{n}}\frac{F\mathbf{n}_0 \otimes F\mathbf{n}_0}{\|F\mathbf{n}_0\|^2}\,.
\tag{2}
$$

Here, $\sigma_{\mathrm{m}}^{\mathrm{l}}$, $\sigma_{\mathrm{m}}^{\mathrm{t}}$ and $\sigma_{\mathrm{m}}^{\mathrm{n}}$ are conductivities in the direction of fibers, sheets and normal to sheets respectively.

The formulations of both the monodomain Equation (1) and the conductivity tensor (2) incorporate the so-called geometry-mediated mechano-electric feedback mechanisms, through the terms J and F[19,31,65,84] that account for the fact that the electrical stimulus is propagating in a deforming medium. We point out that ours is not the only approach to modeling geometry-mediated mechano-electric feedback, regarding both the monodomain Equation (1) and the definition of the conductivity tensor (2). Multiple strategies are compared in Reference [65], finding that different approaches only have mild effects on the numerical results. However, our model does not include other effects such as nonselective stretch-activated currents or mechanically induced calcium release,[85] which may become relevant in pathological conditions.[65]

Finally, I_{app} is a time-dependent forcing term that provides the initial stimulus. We impose an applied current on three points $\widehat{\mathbf{x}}_{\mathrm{app}}^0$, $\widehat{\mathbf{x}}_{\mathrm{app}}^1$ and $\widehat{\mathbf{x}}_{\mathrm{app}}^2$ on the endocardial surface of the ventricle, to trigger the electrical activation (Figure 2A). The applied current has the following analytical expression:

$$
I_{\mathrm{app}}(\widehat{\mathbf{x}},\ t) =
\begin{cases}
\displaystyle\sum_{i=0}^{3} A_{\mathrm{app}} \exp\left\{ -\left(\frac{\|\widehat{\mathbf{x}} - \widehat{\mathbf{x}}_{\mathrm{app}}^i\|}{\sigma_{\mathrm{app}}}\right)^2 \right\} & \text{if } t \in \left(0,\ T_{\mathrm{app}}\right]\,, \\[4mm]
0 & \text{if } t > T_{\mathrm{app}}\,.
\end{cases}
$$

This mimics the effect of the bundle branches, while the cardiac conduction system, including the Purkinje network, is not explicitly modeled.[15,18,20,86,87] The stimulus is repeated every $T_{\mathrm{hb}} = 800$ ms to obtain multiple heartbeats.
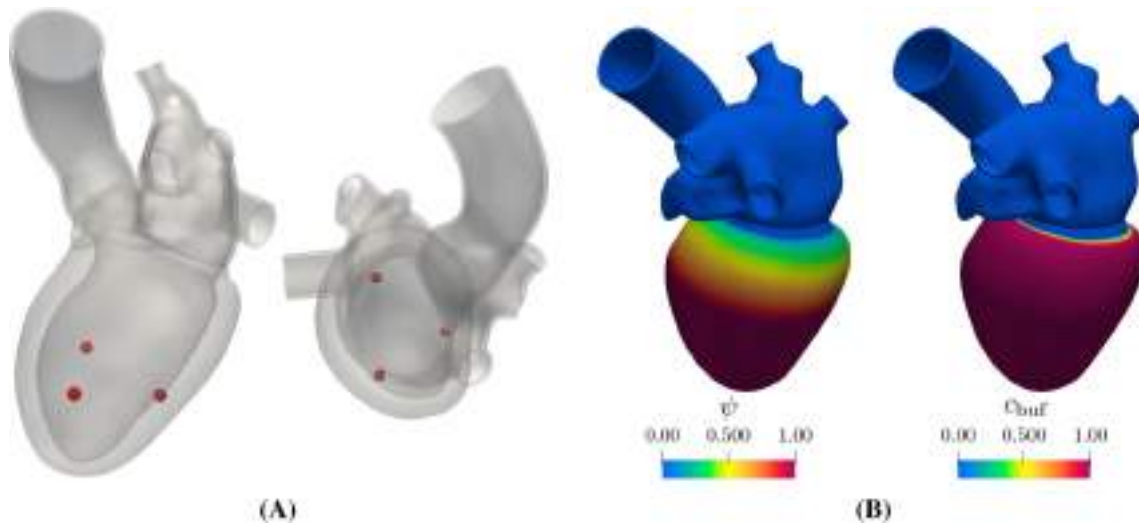
FIGURE 2 (A) Stimulation points (red) on the left ventricular endocardium. (B) Functions ψ (left) and c_{buf} used in the regularization of the interface between ventricle and atrioventricular ring

2.1.3 | Force generation model

In response to the electrical excitation, muscular cells shorten, generating an active contractile force. As done for the electrophysiology, we model the ventricle $\widehat{\Omega}_s^{\text{LV}}$ as actively contracting, whereas all other subdomains are treated as mechanically passive.

We use the activation model RDQ20-MF presented in Reference [66]. The model is biophysically detailed, in the sense that it provides an explicit representation of the subcellular mechanisms leading to the generation of contractile force. Moreover, it includes the feedback between force generation and sarcomere length, responsible for the Frank-Starling mechanism,[8,9,88,89] and between force generation and fiber shortening velocity.[8,90] Both were found to be fundamental in capturing accurately the heart function, especially for what concerns the hemodynamics. Indeed, it was shown in Reference [24] that including the force-velocity relationship is crucial to obtain realistic values for the flowrates through semilunar valves.

The RDQ20-MF model is expressed in terms of a system of ODEs defined at each point of $\widehat{\Omega}_s^{\text{LV}}$:

$$
\begin{cases}
\dfrac{\partial \mathbf{s}}{\partial t} = \mathbf{F}_{\text{act}}\left(\mathbf{s},\ \left[\text{Ca}^{2+}\right]_i,\ SL,\ \dfrac{\partial SL}{\partial t}\right) & \text{in } \widehat{\Omega}_s^{\text{LV}} \times (0,\ T)\ , \\
\mathbf{s} = \mathbf{s}_0 & \text{in } \widehat{\Omega}_s^{\text{LV}} \times \{0\}\ .
\end{cases}
\tag{3}
$$

In the above system, $\mathbf{s}$ is a vector of variables defining the contraction state of cardiac cells, and SL is the sarcomere length, defined as $SL = SL_0\sqrt{I_{4f}}$. SL_0 is the sarcomere length at rest[66] and $I_{4f} = F\mathbf{f}_0 \cdot F\mathbf{f}_0$ is a measure of the stretch along the fibers.

In practice, to compute SL, we solve the following regularization problem:

$$
\begin{cases}
-\delta_{\text{SL}}^2 \Delta\text{SL} + \text{SL} = SL_0\sqrt{I_{4f}} & \text{in } \widehat{\Omega}_s \times (0,\ T)\ , \\
\delta_{\text{SL}}^2 \nabla\text{SL} \times \mathbf{n} = 0 & \text{on } \partial\widehat{\Omega}_s \times (0,\ T)\ ,
\end{cases}
\tag{4}
$$

with δ_{SL} a suitable regularization radius parameter. This has the effect of preventing sharp variations of SL over spatial scales smaller than δ_{SL}[30]

The generated active force is computed at every point $\widehat{\mathbf{x}} \in \widehat{\Omega}_s^{\text{LV}}$ as a function $T_{\text{act}}(\mathbf{s})$ of the contraction state $\mathbf{s}$. For the precise definition of $\mathbf{F}_{\text{act}}$ and T_{act}, we refer to Reference [66]. The force-velocity relationship may yield instabilities, which are prevented with a numerically consistent stabilization as described in Reference [91].

The initial state $\mathbf{s}_0$ is obtained by solving the system (3) uncoupled from the other models, until a steady state solution is reached.

2.1.4 | Solid mechanics

The deformation of the heart wall is modeled in a Lagrangian reference framework with the elastodynamics equation.[92] The vector $\mathbf{d}$ describes the displacement of the solid domain, so that

$$\mathscr{L}_s(\widehat{\mathbf{x}}, t) = \widehat{\mathbf{x}} + \mathbf{d}(\widehat{\mathbf{x}}, t) \quad \widehat{\mathbf{x}} \in \widehat{\Omega}_s, t \in (0, T) .$$

Let $\widehat{\Gamma}_s^{epi} \subset \partial\widehat{\Omega}_s \backslash \widehat{\Sigma}$ be the epicardial boundary, corresponding to the outer wall of the heart, $\widehat{\Gamma}_s^{PV} \subset \partial\widehat{\Omega}_s \backslash \widehat{\Sigma}$ be the portion of the boundary corresponding to the pulmonary veins sections, and $\widehat{\Gamma}_s^{ao} \subset \partial\widehat{\Omega}_s \backslash \widehat{\Sigma}$ be the one corresponding to the AA terminal section (Figure 1B). The equations for solid mechanics read

$$\begin{cases} \rho_s \dfrac{\partial \mathbf{d}}{\partial t^2} - \nabla \cdot P_s(\mathbf{d}, \mathbf{s}) = \mathbf{0} & \text{in } \widehat{\Omega}_s \times (0, T) , \\[2mm] \mathbf{d} = \mathbf{0} & \text{on } \left(\widehat{\Gamma}_s^{PV} \cup \widehat{\Gamma}_s^{ao}\right) \times (0, T) , \\[2mm] P_s(\mathbf{d}, \mathbf{s})\widehat{\mathbf{n}} = -(\widehat{\mathbf{n}} \otimes \widehat{\mathbf{n}})\left(K_\perp^{epi}\mathbf{d} + C_\perp^{epi}\dot{\mathbf{d}}\right) & \\[2mm] \qquad\qquad - (I - \widehat{\mathbf{n}} \otimes \widehat{\mathbf{n}})\left(K_\parallel^{epi}\mathbf{d} + C_\parallel^{epi}\dot{\mathbf{d}}\right) & \text{on } \widehat{\Gamma}_s^{epi} \times (0, T) , \\[2mm] \mathbf{d} = \mathbf{d}_0 & \text{in } \widehat{\Omega}_s \times \{0\} . \end{cases} \quad (5)$$

In the above system, ρ_s is the density of the solid and $P_s(\mathbf{d}, \mathbf{s})$ is the first Piola-Kirchhoff stress tensor. The stress tensor incorporates both the passive and the active mechanical properties of the material. We work in the active stress framework,[7,26,30,93–96] decomposing the stress tensor into the sum of a passive and an active term:

$$P_s(\mathbf{d}, \mathbf{s}) = P_{pas}(\mathbf{d}) + P_{act}(\mathbf{d}, \mathbf{s}) .$$

The passive part is obtained as the derivative of a strain energy function $\mathcal{W}$ that characterizes the mechanical properties of the material[92]:

$$P_{pas}(\mathbf{d}) = \frac{\partial \mathcal{W}}{\partial F} .$$

We use the Guccione anisotropic constitutive law[33,97] in both the ventricle $\widehat{\Omega}_s^{LV}$ and the atrium $\widehat{\Omega}_s^{LA}$. In $\widehat{\Omega}_s^{AA}$ and $\widehat{\Omega}_s^{ring}$ we use an isotropic neo-Hookean material model.[92] In both cases, we treat the solid as nearly incompressible, by penalizing local volume variations in the strain energy function. See Appendix A for the definitions of the constitutive laws.

The active part of the stress tensor is computed as a function of the activation state, through

$$P_{act}(\mathbf{d}, \mathbf{s}) = T_{act}(\mathbf{s}) \frac{F\mathbf{f}_0 \otimes \mathbf{f}_0}{\sqrt{I_{4f}}} .$$

The boundary conditions imposed on the mechanics equations are a homogeneous Dirichlet condition on $\widehat{\Gamma}_s^{PV}$ and $\widehat{\Gamma}_s^{ao}$,[2] and a generalized visco-elastic Robin boundary condition on $\widehat{\Gamma}_s^{epi}$. The latter has the purpose of modeling the presence of the pericardial sac that surrounds the heart and provides mechanical support. For simplicity, in this study homogeneous coefficients $K_\perp^{epi}$, $K_\parallel^{epi}$, $C_\perp^{epi}$ and $C_\parallel^{epi}$ are considered. A more physiologically accurate model employs heterogeneous coefficients, accounting for the different organs surrounding the heart.[28,32] Finally, no boundary conditions are prescribed on $\widehat{\Sigma}$ since the interface conditions for the fluid–solid coupling are set on that portion of $\partial\widehat{\Omega}_s$ (see Section 2.1.7).

Initial conditions

We start from a model of the left heart that corresponds to a configuration reconstructed from CT and MRI scans.[98] Such configuration is subject to the load of blood pressure on the endocardial wall, while the elastodynamics Equation (5) is formulated assuming that $\widehat{\Omega}_s$ is stress-free. Therefore, as a preprocessing step, we compute a stress-free reference configuration using the unloading algorithm presented in Reference [30].

From there, we determine the initial condition for the solid displacement $\mathbf{d}_0$ by solving a quasi-static ramp, as described in Reference [30], imposing an initial pressure p_0 on the endocardial wall. We choose p_0 to match typical values at the end of the diastolic phase. We remark that different initial pressures p_0^{LA}, p_0^{ring}, p_0^{LV} and p_0^{AA} are prescribed on the boundaries of the different chambers.[24]

Material interface regularization

The different material models used result in sharp discontinuities across the interface between the atrioventricular ring subdomain and the atrium and ventricle subdomains. These do not constitute an issue from the point of view of solid mechanics. However, they lead to the formation of corners at the fluid–solid interface, which pose a relevant numerical issue for the fluid domain displacement inducing mesh elements distortion (see Section 2.1.5). To overcome it, we regularize the interface between $\widehat{\Omega}_s^{LV}$ and $\widehat{\Omega}_s^{ring}$ as follows. As a preprocessing step, a Laplace problem is solved to obtain a function ψ that varies smoothly from 0 in $\widehat{\Omega}_s^{ring}$ to 1 in the apical portion of $\widehat{\Omega}_s^{LV}$. We then set

$$c_{buf}(\widehat{\mathbf{x}}) = \frac{1}{2}\left[1 - \cos\left(\frac{\pi \min\{\psi, \ \psi_{th}\}}{\psi_{th}}\right)\right],$$

where ψ_{th} is a threshold value that controls the size of the regularization region. Both ψ and c_{buf} are depicted in Figure 2B. Finally, we redefine the stress tensor in $\widehat{\Omega}_s^{LV}$ as a convex combination of the Guccione (G) and neo-Hookean (NH) stress tensors so that the transition between the material of the ventricle (or the atrium) and the atrioventricular ring is smooth:

$$P_{pas}(\mathbf{d}) = c_{buf} P_G(\mathbf{d}) + (1 - c_{buf}) P_{NH}(\mathbf{d}).$$

This implies that there is a smooth transition between an orthotropic constitutive law and an isotropic one, in the regularization region. The regularization is included at the interfaces between $\widehat{\Omega}_s^{LV}$ and $\widehat{\Omega}_s^{ring}$ and between $\widehat{\Omega}_s^{LA}$ and $\widehat{\Omega}_s^{ring}$.

2.1.5 | Fluid domain displacement

We account for the motion of Ω_f in the arbitrary Lagrangian–Eulerian (ALE) framework.[99,100,101] The vector $\mathbf{d}_{ALE}$ represents the displacement of the fluid domain, such that

$$\mathscr{L}_f(\widehat{\mathbf{x}}, t) = \widehat{\mathbf{x}} + \mathbf{d}_{ALE}(\widehat{\mathbf{x}}, t) \quad \widehat{\mathbf{x}} \in \widehat{\Omega}_f, t \in (0, T).$$

Inspired by References [58,102-104], we use a fictitious non-linear solid material to model the displacement of the fluid domain, so that $\mathbf{d}_{ALE}$ solves at every time t the following stationary problem:

$$\begin{cases} -\nabla \times P_{ALE}(\mathbf{d}_{ALE}) = \mathbf{0} & \text{in } \widehat{\Omega}_f, \\ \mathbf{d}_{ALE} = \mathbf{d} & \text{on } \widehat{\Sigma}, \\ \mathbf{d}_{ALE} = \mathbf{0} & \text{on } \widehat{\Gamma}_f^{PV} \cup \widehat{\Gamma}_f^{ao}, \end{cases} \tag{6}$$

Where in[103,104]

$$P_{\text{ALE}} = \frac{1}{q}\left(I - \left(F_{\text{ALE}}F_{\text{ALE}}^T\right)^{-1}\right) ,$$
$$F_{\text{ALE}} = I + \mathbf{d}_{\text{ALE}} .$$

In the above, q is a scale-invariant mesh quality metric that has the purpose of stiffening the regions of the fluid domain with highly distorted element, aiming at preventing solver breakdown. It is defined element-wise as

$$q(\widehat{\mathbf{x}}) = \frac{|D_{\text{ALE}}|_{\text{F}}^2}{3(\det D_{\text{ALE}})^{\frac{2}{3}}} ,$$

where $D_{\text{ALE}} = F_{\text{ALE}}\nabla\mathcal{M}$ and $\mathcal{M}$ is the linear mapping from the unit simplex to the element in current configuration.

We remark that (6) is non-linear, since P_{ALE} is a non-linear function of $\mathbf{d}_{\text{ALE}}$. Therefore, its solution is significantly more complex and costly than that of other typically used operators, such as the harmonic extension operator[43,52,67] or linear elasticity.[101,105] On the other hand, however, we found that this results in an increased robustness with respect to large deformations, preventing the inversion of mesh elements, that would result in the breakdown of the numerical solver. Indeed, for our numerical experiments, harmonic extension or linear elastic operators were not robust enough, even when including Jacobian- or boundary-based stiffening.[106,101]

We define the ALE velocity as the time derivative of $\mathbf{d}_{\text{ALE}}$, pushed forward to the current configuration, namely

$$\mathbf{u}_{\text{ALE}}(\mathbf{x}, t) = \frac{\partial \mathbf{d}_{\text{ALE}}}{\partial t}\left(\mathscr{L}_{\text{f}}^{-1}(\mathbf{x}, t), t\right) .$$

2.1.6 | Fluid dynamics

The evolution of fluid velocity $\mathbf{u}$ and pressure p is prescribed by the Navier–Stokes equations for a Newtonian, incompressible fluid[71]:

$$\begin{cases} \rho_{\text{f}}\left[\dfrac{\partial \mathbf{u}}{\partial t} + ((\mathbf{u} - \mathbf{u}_{\text{ALE}}) \times \nabla)\mathbf{u}\right] - \nabla \times \sigma_{\text{f}}(\mathbf{u}, p) + \mathscr{R}(\mathbf{u}, \mathbf{u}_{\text{ALE}}) = \mathbf{0} & \text{in } \Omega_{\text{f}} \times (0, T), \\ \nabla \times \mathbf{u} = 0 & \text{in } \Omega_{\text{f}} \times (0, T), \\ \sigma_{\text{f}}(\mathbf{u}, p)\mathbf{n} = -p_{\text{in}}(t)\mathbf{n} & \text{on } \Gamma_{\text{f}}^{\text{PV}} \times (0, T), \\ \sigma_{\text{f}}(\mathbf{u}, p)\mathbf{n} = -p_{\text{out}}(t)\mathbf{n} & \text{on } \Gamma_{\text{f}}^{\text{ao}} \times (0, T), \\ \mathbf{u} = \mathbf{0} & \text{in } \Omega_{\text{f}} \times \{0\}. \end{cases} \quad (7)$$

In the above system, ρ_{f} denotes the fluid density, and the stress tensor σ_{f} is given by

$$\sigma_{\text{f}}(\mathbf{u}, p) = \mu_{\text{f}}\left(\nabla\mathbf{u} + \nabla\mathbf{u}^T\right) - pI ,$$

where μ_{f} is the dynamic viscosity. $\mathscr{R}(\mathbf{u})$ is a resistive term that accounts for the presence of valves in a penalty-based approach (see below).[43,107–111]

In analogy with the solid mechanics problem (Section 2.1.4), no boundary conditions are prescribed on Σ since, on that portion of $\partial\Omega_{\text{f}}$, the interface conditions for the fluid–solid coupling are imposed (see Section 2.1.7). The functions $p_{\text{in}}(t)$ and $p_{\text{out}}(t)$ are pressures provided by the circulation model (see Section 2.1.8) for the pulmonary venous and systemic arterial circulation compartments, respectively.

Valve modeling

Heart compartments are separated by valves that prevent reverse flow.[8] For a left heart model, the mitral valve (MV) separates the LV and the LA, and the aortic valve (AV) separates the LV and the AA. Accurate modeling and numerical simulation of the valves is challenging: the valves are thin structures, they undergo large displacements, and contact phenomena play a major role in their physiological function.[45,48,112–117] Our interest mainly lies in the macroscopic effect of the opening and closing of the valves onto the blood flow, rather than on an accurate description of valves motion. In particular, we want our model to describe the role of valves in ensuring the correct direction of the flow through the heart, and to capture the formation of jets and vortices associated to the presence of valve leaflets.

Therefore, we use a reduced approach for the modeling of valves, based on the Resistive Immersed Implicit Surface (RIIS) method.[43,69,108–110] Each valve, at any time $t \in (0, T)$, is represented by a surface Γ_k^t, $k \in \{MV, AV\}$, immersed in the fluid domain. For $k \in \{MV, AV\}$, let $\varphi_k^t(\mathbf{x})$ be the signed distance function from the surface Γ_k^t. The Navier–Stokes momentum Equation (7) includes the penalization term $\mathscr{R}(\mathbf{u}, \mathbf{u}_{ALE})$ forcing the fluid velocity to match the valve velocity (with respect to the moving frame of the domain) near the immersed surfaces:

$$\mathscr{R}(\mathbf{u}, \mathbf{u}_{ALE}) = \sum_{k \in \{MV, AV\}} \frac{R_k}{\varepsilon_k} \delta_{\varepsilon_k}\left(\varphi_k^t(\mathbf{x})\right)\left(\mathbf{u} - \mathbf{u}_{ALE} - \mathbf{u}_{\Gamma_k}\right) .$$

In the above, R_k are resistance parameters, ε_k are valves half-thicknesses, $\mathbf{u}_{\Gamma_k}$ is the valve velocity with respect to the moving domain, and δ_{ε_k} is a smoothed delta function, defined as

$$\delta_{\varepsilon_k}(y) = \begin{cases} \left(\frac{1}{2\varepsilon_k}\left(1 + \cos\left(\frac{\pi y}{\varepsilon_k}\right)\right)\right) & \text{if} |y| \leq \varepsilon_k , \\ 0 & \text{if} |y| > \varepsilon_k . \end{cases}$$

We account for the opening and closing of valves by deforming the corresponding surfaces. Although we do not include any FSI model for the valves, their opening and closing times are determined based on the pressure jump across the immersed surfaces while the durations of opening and closing are prescribed. We refer to Reference [43] and Appendix B for more details.

Flow stabilization and turbulence modeling

Blood flow in the heart chambers is characterized by a regime of transition to turbulence.[42,43,118–120] To account for that, we use the VMS-LES model for fine scales.[42,121] We refer the interested reader to Reference [121] for details on the VMS-LES approach to turbulence modeling. We remark that, with respect to the original formulation, the stabilization terms and stabilization parameters are modified to account for the RIIS method, as presented in Reference [43].

We set Neumann boundary conditions on boundaries Γ_f^{PV} and Γ_f^{ao}. Neumann conditions may cause instability phenomena in case of inflow.[122,123] Therefore, we make use of backflow stabilization in the form of inertial stabilization as presented in Reference [122]: Neumann boundary conditions are modified by imposing

$$\begin{cases} \sigma_f(\mathbf{u}, p)\mathbf{n} = -p_{in}(t)\mathbf{n} + \beta\frac{\rho_f}{2}|\mathbf{u} \times \mathbf{n}|_- \mathbf{u} & \text{on } \Gamma_f^{PV} \times (0, T) , \\ \sigma_f(\mathbf{u}, p)\mathbf{n} = -p_{out}(t)\mathbf{n} + \beta\frac{\rho_f}{2}|\mathbf{u} \times \mathbf{n}|_- \mathbf{u} & \text{on } \Gamma_f^{ao} \times (0, T) , \end{cases}$$

where $|\mathbf{u} \times \mathbf{n}|_- = \min\{\mathbf{u} \times \mathbf{n}, 0\}$ and $\beta = 1$.

2.1.7 | Fluid–structure interaction

The fluid and solid models are coupled by kinematic and dynamic interface conditions on Σ that prescribe the continuity of velocity and of stresses[67,124]:

$$\begin{cases} \mathbf{u} = \mathbf{d}t & \text{on } \Sigma \times (0, \ T) , \\ \sigma_{\mathrm{f}}(\mathbf{u}, \ p)\mathbf{n} = \sigma_{\mathrm{s}}(\mathbf{d}, \ \mathbf{s})\mathbf{n} & \text{on } \Sigma \times (0, \ T) . \end{cases}$$

In the above, $\sigma_{\mathrm{s}}(\mathbf{d})$ is the Cauchy stress tensor for the solid, related to the first Piola-Kirchhoff tensor by

$$J\sigma_{\mathrm{s}}(\mathbf{d}, \mathbf{s}) = \mathrm{F}P_{\mathrm{s}}(\mathbf{d}, \mathbf{s})^T .$$

2.1.8 | Circulation model

Inlet and outlet conditions for the fluid model are provided by a zero-dimensional circulation model,[30,43,68,125] representing the whole closed-loop circulation with a lumped-parameter approach. The model includes four different circulation compartments (systemic arterial, systemic venous, pulmonary arterial and pulmonary venous) as well as the four heart chambers. Using an electric circuit analogy[68] represented in Figure 3, the circulation compartments are modeled as RLC circuits, heart chambers are modeled as time-varying elastances, and valves are modeled as non-ideal diodes.

In order to couple it to the three-dimensional FSI model, we remove from the full circulation model those compartments that have a three-dimensional description, that is the left atrium, the left ventricle, and mitral and aortic valves.[43] The remaining unknowns are the volumes and pressures of the right atrium and ventricle (V_{RA}, p_{RA}, V_{RV} and p_{RV}), pressures and flow rates through the four circulation compartments, except for the pulmonary venous flow rate ($p_{\mathrm{AR}}^{\mathrm{SYS}}$, $Q_{\mathrm{AR}}^{\mathrm{SYS}}$, $p_{\mathrm{VEN}}^{\mathrm{SYS}}$, $Q_{\mathrm{VEN}}^{\mathrm{SYS}}$, $p_{\mathrm{AR}}^{\mathrm{PUL}}$, $Q_{\mathrm{AR}}^{\mathrm{PUL}}$ and $p_{\mathrm{VEN}}^{\mathrm{PUL}}$), and flow rates through tricuspid and pulmonary valves (Q_{PV} and Q_{TV}). Collecting all the circulation variables into the vector $\mathbf{c}(t)$, the circulation problem can be stated in compact form as a differential-algebraic equation:

$$\mathbf{F}_{\mathrm{circ}}\left(\frac{\partial \mathbf{c}}{\partial t}, \mathbf{c}, t\right) = \mathbf{0} .$$

Refer to Appendix C for the definition of $\mathbf{F}_{\mathrm{circ}}$.

Following,[126,43] the 0D circulation model is coupled to the 3D fluid model by imposing the continuity of stresses and of fluxes at the 3D-0D interface: for $t \in (0, \ T)$,
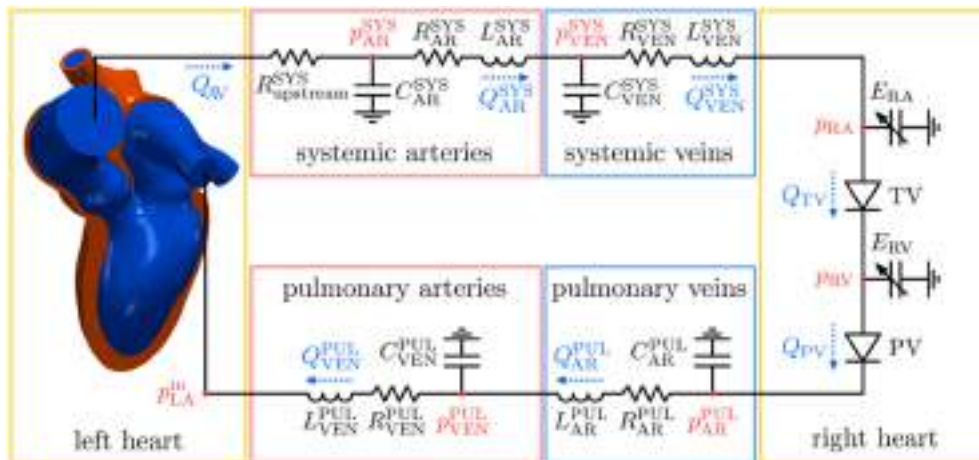

FIGURE 3 Circuital (0D) representation for the circulation model coupled to the electrophysiology-mechanics-fluid dynamics (EMF) model. Refer to Appendix C for the model equations

$$p_{\text{in}}(t) = p_{\text{LA}}^{\text{in}}(t) \ ,$$
$$p_{\text{out}}(t) = p_{\text{AR}}^{\text{SYS}}(t) + R_{\text{upstream}}^{\text{SYS}} Q_{\text{AV}}(t) \ ,$$
$$Q_{\text{VEN}}^{\text{PUL}}(t) = - \int_{\Gamma_f^{\text{PV}}} (\mathbf{u} - \mathbf{u}_{\text{ALE}}) \times \mathbf{n} d\gamma \ ,$$
$$Q_{\text{AV}}(t) = \int_{\Gamma_f^{\text{ao}}} (\mathbf{u} - \mathbf{u}_{\text{ALE}}) \times \mathbf{n} d\gamma \ .$$

A derivation of the flowrate coupling conditions can be found in Appendix C.1. We remark that, with respect to Reference [43], we include the resistance term $R_{\text{upstream}}^{\text{SYS}} Q_{\text{AV}}(t)$ when coupling the outlet to the systemic arterial compartment. This has the role of avoiding reflections of pressure waves at the outlet, that would otherwise result in unphysical oscillations.[127] $p_{\text{LA}}^{\text{in}}(t)$ is the pressure downstream of the pulmonary veins compartment (Figure 3). We remark that we are imposing the same pressure on all pulmonary vein inlets. Although this approach is common in the cardiac modeling literature,[4,40,69] different pressures at the different pulmonary veins could be imposed through suitable modifications of the lumped parameter model.

2.2 | Numerical discretization

We detail the discretization strategy used to numerically solve the fully coupled EMF problem, starting from the semi-discretization in time (Section 2.2.1) and then describing spatial discretization (Section 2.2.2).

2.2.1 | Time discretization

We introduce a partition of the time interval $(0, T)$ into sub-intervals $(t_i, t_{i+1}]$, with $i = 0, 1, \ldots, N_T$, $t_0 = 0$ and $t_{N_T} = T$, and such that $t_{i+1} - t_i = \Delta t$ for all i. From here on, we denote the approximation of any of the solution variables at a given timestep t_n with the superscript n, for example, $\mathbf{u}^n \approx \mathbf{u}(t_n)$.

We employ a staggered scheme for the coupling of the different systems of equations, schematically represented in Figure 4. The scheme is based on solving separately the different subproblems, using an explicit coupling whenever stability is not a concern. We remark that we use an implicit coupling of the FSI problem.[67] The scheme is derived from
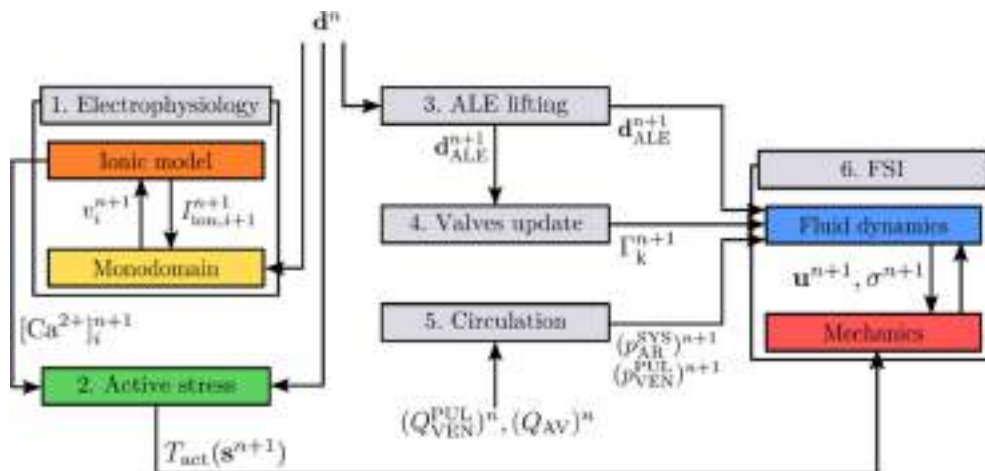

FIGURE 4 Time advancing scheme for the coupled model. The numbers correspond to the steps described in Section 2.2.1.

that in Reference [30] for the electromechanics of the left ventricle, adapted to include the three dimensional description of the blood hemodynamics.

We use finite differences for the approximation of time derivatives appearing in the different model equations. Electrophysiology is characterized by a faster dynamics than the other models, and requires a smaller timestep for an accurate solution.[30] Therefore, we discretize it with a timestep $\Delta t_{EP} = \frac{\Delta t}{N_{EP}}$, with $N_{EP} \in \mathbb{N}$. Given the solution variables and the domain Ω_f^n at timestep t_n, in order to compute the solution at timestep t_{n+1} we perform the following steps:

1. Electrophysiology: we solve N_{EP} time advancing steps of the electrophysiology problem, that is: setting $v_0^{n+1} = v^n$ and $\mathbf{w}_0^{n+1} = \mathbf{w}^n$, for $i = 0,1,\dots,N_{EP} - 1$:
   a. we compute $\mathbf{w}_{i+1}^{n+1}$ and $\mathbf{z}_{i+1}^{n+1}$ by solving the ionic model
   b.

$$
\begin{cases}
\dfrac{\mathbf{w}_{i+1}^{n+1} - \mathbf{w}_i^{n+1}}{\Delta t_{EP}} = \mathbf{F}_{ion}^{\mathbf{w}}\left(v_i^{n+1},\ \mathbf{w}_{i+1}^{n+1}\right) & \text{in}\,\widehat{\Omega}_s^{LV}\,, \\[2mm]
\dfrac{\mathbf{z}_{i+1}^{n+1} - \mathbf{z}_i^{n+1}}{\Delta t_{EP}} = \mathbf{F}_{ion}^{\mathbf{z}}\left(v_i^{n+1},\ \mathbf{w}_i^{n+1},\ \mathbf{z}_{i+1}^{n+1}\right) & \text{in}\,\widehat{\Omega}_s^{LV}\,.
\end{cases}
\tag{8}
$$

We use an implicit-explicit (IMEX) scheme, with an implicit discretization of gating variables and an explicit discretization of ionic concentrations.[128,30]
   c. Then, we solve the monodomain equation to compute v_{i+1}^{n+1}:
   d.

$$
\begin{cases}
J^n \chi C_m \dfrac{v_{i+1}^{n+1} - v_i^{n+1}}{\Delta t_{EP}} - \nabla \cdot \left(J^n (F^n)^{-1} D_m (F^n)^{-T} \nabla v_{i+1}^{n+1}\right) & \text{in}\,\widehat{\Omega}_s^{LV}\,, \\[2mm]
\quad + J^n \chi I_{ion}\left(v_i^{n+1},\ \mathbf{w}_{i+1}^{n+1},\ \mathbf{z}_{i+1}^{n+1}\right) = J^n \chi I_{app}\left(\widehat{\mathbf{x}},\ t^n + (i+1)\Delta t_{EP}\right) & \\[2mm]
J^n (F^n)^{-1} D_m (F^n)^{-T} \nabla v_{i+1}^{n+1} \cdot \widehat{\mathbf{n}} = 0 & \text{on}\,\partial\widehat{\Omega}_s^{LV}\,.
\end{cases}
\tag{9}
$$

   e. System (9) relies on a semi-implicit discretization, since the ionic current term is computed using the tramsmembrane potential at previous subiteration, v_i^{n+1}. Therefore, the problem is linear.
   f. We set $v^{n+1} = v_{N_{EP}}^{n+1}$, $\mathbf{w}^{n+1} = \mathbf{w}_{N_{EP}}^{n+1}$ and $\mathbf{z}^{n+1} = \mathbf{z}_{N_{EP}}^{n+1}$;
2. Force generation model: we compute SL^n solving (4) using $\mathbf{d}^n$ to compute I_{4f}, then we solve the activation model to compute $\mathbf{s}^{n+1}$
   a.

$$
\frac{\mathbf{s}^{n+1} - \mathbf{s}^n}{\Delta t} = \mathbf{F}_{act}\left(s^n,\ \left[Ca^{2+}\right]_i^{n+1},\ SL^n,\ \frac{SL^n - SL^{n-1}}{\Delta t}\right).
\tag{10}
$$

3. Fluid domain displacement: we compute $\mathbf{d}_{ALE}^{n+1}$ by solving
   a.

$$
\begin{cases}
-\nabla \cdot P_{ALE}\left(\mathbf{d}_{ALE}^{n+1}\right) = \mathbf{0} & \text{in}\,\widehat{\Omega}_f\,, \\[2mm]
\mathbf{d}_{ALE}^{n+1} = \mathbf{d}^n & \text{on}\,\widehat{\Sigma}\,, \\[2mm]
\mathbf{d}_{ALE}^{n+1} = \mathbf{0} & \text{on}\,\widehat{\Gamma}_f^{PV} \cup \widehat{\Gamma}_f^{ao}\,.
\end{cases}
\tag{11}
$$

We remark that we compute $\mathbf{d}_{ALE}^{n+1}$ from the displacement $\mathbf{d}^n$ from the previous timestep, so that the geometric FSI coupling condition is treated explicitly. We then update the fluid domain Ω_f^{n+1} according to the displacement $\mathbf{d}_{ALE}^{n+1}$ and compute

$$\mathbf{u}_{\mathrm{ALE}}^{n+1}(\mathbf{x}) = \frac{\mathbf{d}_{\mathrm{ALE}}^{n+1}\left(\left(\mathscr{L}_{\mathrm{f}}^{n+1}\right)^{-1}(\mathbf{x})\right) - \mathbf{d}_{\mathrm{ALE}}^{n}\left(\left(\mathscr{L}_{\mathrm{f}}^{n}\right)^{-1}(\mathbf{x})\right)}{\Delta t} ;$$

4. Valves position: we update the position of the valves according to their opening state and to $\mathbf{d}_{\mathrm{ALE}}^{n+1}$, computing the surfaces $\Gamma_{\mathrm{MV}}^{n+1}$ and $\Gamma_{\mathrm{AV}}^{n+1}$ (see Appendix B);
5. Circulation: we compute the flow rates at the 3D-0D interface as

$$\left(Q_{\mathrm{VEN}}^{\mathrm{PUL}}\right)^{n+1} = -\int_{\Gamma_{\mathrm{f}}^{\mathrm{PV}}} \left(\mathbf{u}^n - \mathbf{u}_{\mathrm{ALE}}^{n+1}\right) \times \mathbf{n} d\gamma ,$$

$$Q_{\mathrm{AV}}^{n+1} = \int_{\Gamma_{\mathrm{f}}^{\mathrm{ao}}} \left(\mathbf{u}^n - \mathbf{u}_{\mathrm{ALE}}^{n+1}\right) \times \mathbf{n} d\gamma ,$$

then advance the circulation model (2.1.8) with an explicit Runge–Kutta scheme,[71] to compute $\mathbf{c}^{n+1}$;

6. Fluid–structure interaction: we solve the FSI problem to compute $\mathbf{d}^{n+1}, \mathbf{u}^{n+1}, p^{n+1}$

$$
\begin{cases}
\rho_{\mathrm{f}} \dfrac{\mathbf{d}^{n+1} - 2\mathbf{d}^n + \mathbf{d}^{n-1}}{\Delta t^2} - \nabla \cdot P_{\mathrm{s}}\left(\mathbf{d}^{n+1}, \ \mathbf{s}^{n+1}\right) = \mathbf{0} & \text{in } \widehat{\Omega}_{\mathrm{s}}, \\[2mm]
\mathbf{d}^{n+1} = \mathbf{0} & \text{on } \widehat{\Gamma}_{\mathrm{s}}^{\mathrm{PV}} \cup \widehat{\Gamma}_{\mathrm{s}}^{\mathrm{ao}}, \\[2mm]
P_{\mathrm{s}}\left(\mathbf{d}^{n+1}, \ \mathbf{s}^{n+1}\right)\widehat{\mathbf{n}} = -\left(\widehat{\mathbf{n}} \bigotimes \widehat{\mathbf{n}}\right)\left(K_{\perp}^{\mathrm{epi}}\mathbf{d}^{n+1} + C_{\perp}^{\mathrm{epi}}\dfrac{\mathbf{d}^{n+1} - \mathbf{d}^n}{\Delta t}\right) & \\[2mm]
\quad -\left(I - \widehat{\mathbf{n}} \bigotimes \widehat{\mathbf{n}}\right)\left(K_{\parallel}^{\mathrm{epi}}\mathbf{d}^{n+1} + C_{\parallel}^{\mathrm{epi}}\dfrac{\mathbf{d}^{n+1} - \mathbf{d}^n}{\Delta t}\right) & \text{on } \widehat{\Gamma}_{\mathrm{s}}^{\mathrm{epi}}, \\[2mm]
\rho_{\mathrm{f}}\left[\dfrac{\mathbf{u}^{n+1} - \mathbf{u}^n}{\Delta t} + \left(\left(\mathbf{u}^{n+1} - \mathbf{u}_{\mathrm{ALE}}^{n+1}\right)\cdot\right)\mathbf{u}^{n+1}\right] & \text{in } \Omega_{\mathrm{f}}, \\[2mm]
\quad -\nabla \cdot \sigma_{\mathrm{f}}\left(\mathbf{u}^{n+1}, \ p^{n+1}\right) + \mathcal{R}\left(\mathbf{u}^{n+1}, \ \mathbf{u}_{\mathrm{ALE}}^{n+1}\right) = 0 & \\[2mm]
\nabla \cdot \mathbf{u}^{n+1} = 0 & \text{in } \Omega_{\mathrm{f}}, \\[2mm]
\sigma_{\mathrm{f}}\left(\mathbf{u}^{n+1}, \ p^{n+1}\right)\mathbf{n} = -\left(p_{\mathrm{VEN}}^{\mathrm{PUL}}\right)^{n+1}\mathbf{n} + \rho_{\mathrm{f}}\dfrac{\beta}{2}|\mathbf{u}^{n+1}\cdot\mathbf{n}|_{-}\mathbf{u}^{n+1} & \text{on } \Gamma_{\mathrm{f}}^{\mathrm{PV}}, \\[2mm]
\sigma_{\mathrm{f}}\left(\mathbf{u}^{n+1}, \ p^{n+1}\right)\mathbf{n} = -\left(p_{\mathrm{AR}}^{\mathrm{SYS}}\right)^{n+1}\mathbf{n} + \rho_{\mathrm{f}}\dfrac{\beta}{2}|\mathbf{u}^{n+1}\cdot\mathbf{n}|_{-}\mathbf{u}^{n+1} & \text{on } \Gamma_{\mathrm{f}}^{\mathrm{ao}}, \\[2mm]
\mathbf{u}^{n+1} = \dfrac{\mathbf{d}^{n+1} - \mathbf{d}^n}{\Delta t} & \text{on } \Sigma, \\[2mm]
\sigma_{\mathrm{f}}\left(\mathbf{u}^{n+1}, \ p^{n+1}\right)\mathbf{n} = \sigma_{\mathrm{s}}\left(\mathbf{d}^{n+1}, \ \mathbf{s}^{n+1}\right)\mathbf{n} & \text{on } \Sigma.
\end{cases} \tag{12}
$$

For our numerical simulations, we set $\Delta t = 0.2\,\mathrm{ms}$ and $N_{\mathrm{EP}} = 2$, so that $\Delta t_{\mathrm{EP}} = 0.1$ ms.

2.2.2 | Space discretization

We introduce a tetrahedral mesh in both domains $\widehat{\Omega}_{\mathrm{s}}$ and $\widehat{\Omega}_{\mathrm{f}}$, represented in Figure 5A,B. At their interface $\widehat{\Sigma}$, the fluid and solid meshes are conforming. The mesh $\widehat{\Omega}_{\mathrm{f}}$ is updated following the displacement $\mathbf{d}_{\mathrm{ALE}}$, resulting in a tetrahedral mesh over the domain Ω_{f}. The spatial discretization is finer in the region near the valves, to allow better capturing their presence. We report details about the mesh size and number of elements in Table 1.
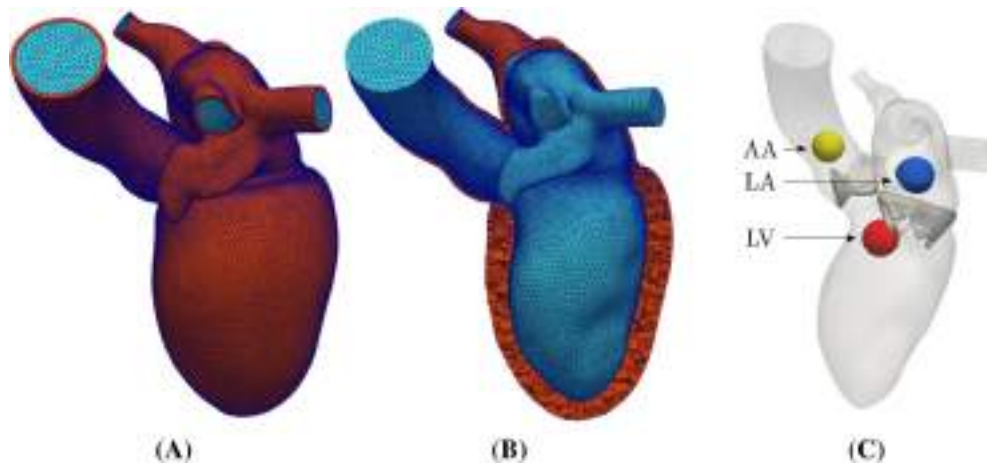
FIGURE 5 (A,B) Computational mesh used for the solid (red) and the fluid (blue) domains. (C) Spherical control volumes used in estimating the average pressures within each chamber. Average pressure within control volumes is also used to trigger the opening and closing of valves

TABLE 1 Minimum, average and maximum mesh element diameter, number of elements and number of nodes used for spatial discretization

	$h_{\min}$ (mm)	h_{avg} (mm)	$h_{\max}$ (mm)	# elem.	# nodes
Fluid	0.51	1.6	4.7	790,533	137,504
Solid	0.59	2.1	5.7	234,132	63,834

The time-discrete ionic model (8) is solved at every vertex in the solid mesh. Then, ionic current $I_{\text{ion}}(v, \mathbf{w}, \mathbf{z})$ is evaluated at every mesh vertex, and interpolated on quadrature nodes of the mesh. This approach is referred to as *ionic current interpolation* (ICI) in the literature.[129,130]

We discretize in space the electrophysiology model (9) with piecewise quadratic finite elements.[70,71] Indeed, quadratic finite elements have been shown to provide improved accuracy with a lower number of degrees of freedom, with respect to linear elements, for cardiac electrophysiology.[131] Since the ionic current term is known from the solution of the ionic model, the resulting problem is linear and symmetric. We solve it with the conjugate gradient (CG) method,[71,132] preconditioned with an algebraic multigrid (AMG) preconditioner.[133] We point out that, in principle, while we do not consider it in this work, a staggered scheme may allow to use a finer spatial discretization for the electrophysiology problem, e.g. by using intergrid transfer operators as presented in Reference [134]. Monodomain conductivities were calibrated to obtain physiological conduction velocities and activation times for the chosen mesh resolution and polynomial degree.

The system (10) is solved at every node in the computational mesh. The regularization problem (4) is solved by means of linear finite elements, using a regularization radius δ_{SL} proportional to the mesh size. The resulting linear system is solved with the CG method, using AMG preconditioning.

The ALE lifting problem (11) is discretized in space with piecewise linear finite elements. The resulting problem is linearized with Newton's method and then solved with the GMRES method,[71,132] preconditioned with AMG.

The FSI problem (12) is discretized monolithically, using condensation of interface variables.[51,52,54,67] We found that the monolithic approach is computationally more efficient and robust with respect to partitioned approaches based on subiterations between the fluid and the solid models, as detailed in Reference [67]. Piecewise linear finite elements are used for the discretization of fluid velocity, fluid pressure and solild displacement. The use of VMS-LES model for the fluid equations yields a stable numerical solution even though linear finite element spaces for pressure and velocity do not fulfill the inf-sup condition.[71] The VMS-LES model also provides stabilization for the advection-dominated regime.[121] The resulting problem is linearized with Newton's method, and solved with the GMRES method, using a block lower-triangular preconditioner described in Reference [67].

3 | NUMERICAL RESULTS AND DISCUSSION

We run numerical simulations on a left heart model provided by Zygote Media Group,[98] representing the heart of an average 21-year-old male. Preprocessing of the geometry was done using the algorithms presented in Reference [135] as implemented in the software library VMTK.[136] Solvers for the individual core models and for the coupled model were implemented in the C++ library life$^\text{x}$,[72–74] based on the finite element core deal.II.[137–139] We run the simulations using 192 parallel processes on the GALILEO100 supercomputer[i] at the CINECA high-performance computing center (Italy).

We simulate three heartbeats, setting $T = 3T_\text{hb} = 2.4$ s, and consider only the last heartbeat in our analysis (starting at $t_0 = 2T_\text{hb} = 1.6$ s), to reduce the effect of initial conditions. Starting from the beginning of the third heartbeat, a periodic limit cycle is reached in terms of ventricular and atrial volumes and pressures. We shall denote with $t_\text{hb} = t - t_0$ times relative to the third heartbeat.

For each heartbeat, the simulation takes approximately 21 h of wall time, 92% of which is spent assembling and solving the FSI problem, 6% assembling and solving the ALE lifting problem and 2% assembling and solving the electrophysiology problem. The force generation model only requires 0.2% of the total wall time.

We found that the computational time associated to the ALE lifting is considerably higher using the non-linear problem (6) than using simpler harmonic or linear elastic lifting operators[101] (for which the wall time would be less than 1% of the total). However, the latter frequently lead to mesh element inversion and solver breakdown, whereas the non-linear operator we employ has proven to be much more robust with respect to deformations. Therefore, we deem the extra computational cost to be justified by the increased reliability of the solver.

For post-processing, we compute the average pressure of each compartment (LA, LV, AA) by averaging the pressure inside a spherical control volume within that compartment (see Figure 5C). In Figure 6, we report the average pressure, volume and volume derivative over time of the compartments. Table 2 collects some quantitative indicators for the heart function, comparing the values obtained by our simulation with data from the medical literature. Our numerical results are consistent with the clinically measured ranges. In the following sections, we provide details on the simulation results for each of the four heartbeat phases (identified in the plots of Figure 6).
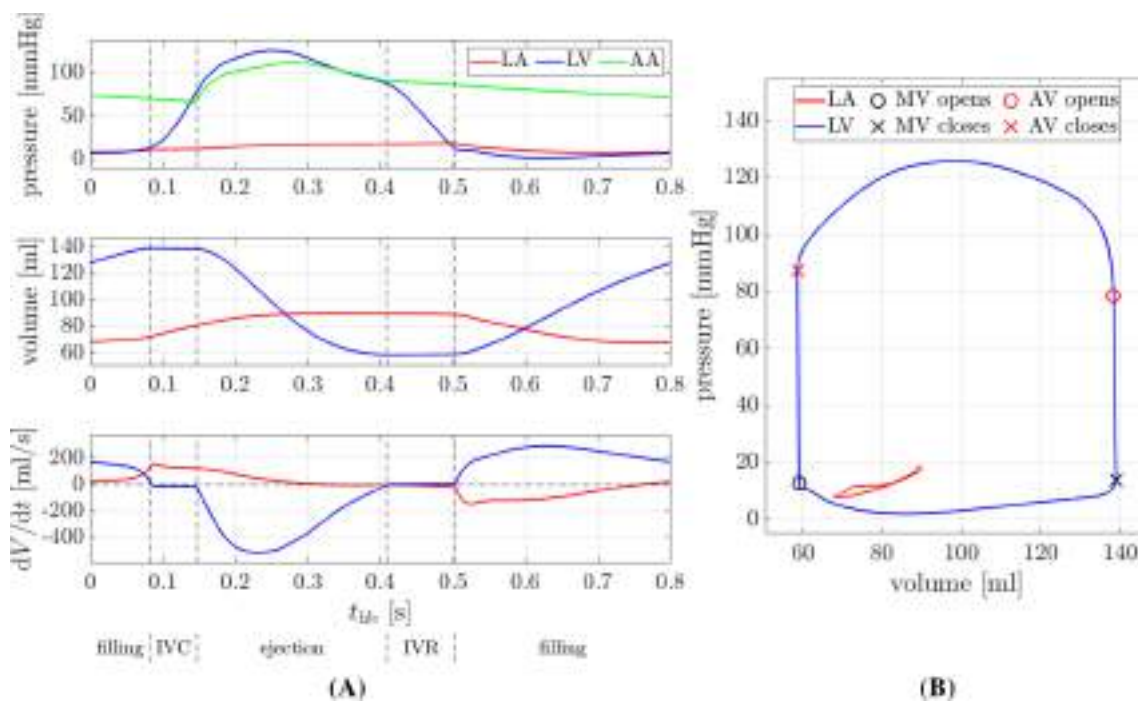

FIGURE 6 (A) Evolution, over the third simulated heartbeat, of the pressure p, volume V and volume derivative dV/dt for the left heart compartments. Vertical dashed lines separate heartbeat phases, labeled on the bottom. (B) Pressure-volume loops for the left ventricle and atrium, with marks indicating opening and closing of valves

TABLE 2 Values of physiological indicators computed from simulation results, and associated normal values from the medical literature

Indicator	Simulation	Normal values		Description
EDV (ml)	139.1	126–208	[140]	Left-ventricular end-diastolic volume
ESV (ml)	58.6	35–80	[140]	Left-ventricular end-systolic volume
SV (ml)	80.4	81–137	[140]	Left-ventricular stroke volume
EF (%)	57.8	49–73	[141]	Left-ventricular ejection fraction
p_{max}^{LV} (mmHg)	126.0	119 ± 13	[142]	Left-ventricular peak systolic pressure
Q_{max}^{AV} (ml/s)	510.0	427 ± 129	[143]	Peak-systolic aortic flow rate
T_{IVC} (ms)	64.2	51–90	[144]	Isovolumetric contraction time
T_{ej} (ms)	261.0	230–334	[144]	Ejection time
T_{IVR} (ms)	94.2	50–140	[145]	Isovolumetric relaxation time
T_{fil} (ms)	379.0	280–472	[146]	Diastolic filling time
LFS (%)	17.8	13–21	[147]	Longitudinal fractional shortening

Note: We report either normal ranges or mean $\pm$ standard deviation.

3.1 | Isovolumetric contraction

The heartbeat starts from the end of the diastolic filling phase, with the MV open and the AV closed (see Figure 6). The electrical stimulus is applied to the activation points of the left ventricle (see Section 2.1.2), leading to it being completely activated within $t_{hb} = 100$ (Figure 7A). This leads to the increase of intracellular calcium concentration (Figure 7D), which subsequently determines the generation of contractile force within the ventricular wall (Figure 7B). Intraventricular pressure rises, triggering the closure of the MV. When the valve is closed ($t_{hb} = 89$ ms), the ventricle is at its *end-diastolic volume* EDV = 139 ml.

At this point, the *isovolumetric contraction* (IVC) phase starts: both valves are closed, and the ventricular pressure increases rapidly (see Figures 6 and 7F) while the volume is maintained approximately constant. Our model does not capture exactly the conservation of ventricular blood volume during this phase, due to the explicit discretization of the fluid domain displacement (11) and to the use of the resistive model for valves, which allows for a little flow through the immersed surfaces. Nonetheless, during isovolumetric contraction the maximum volume variation equals 0.7 ml, corresponding to 0.5% of the EDV. We deem this spurious variation to be acceptable, in accordance with similar spurious variations observed in the cardiac modeling literature.[59]

During the IVC phase, the ventricle undergoes a small deformation, with its shape becoming slightly more spherical (see Figure 7B,E) as described in Reference [8,148].

The IVC phase lasts for $T_{IVC} = 64.2$ ms, consistently with physiological behavior.[144,149] When the pressure in the ventricle becomes larger than the pressure in the aorta, the opening of the AV is triggered and the ejection phase starts.

We remark that the possibility of including isovolumetric phases in a three-dimensional hemodynamics model is distinctive of FSI,[67] as those phases cannot be represented by electromechanics-driven CFD models,[43] unless ad-hoc techniques are implemented.[40,69]

3.2 | Ejection

Blood is ejected from the ventricle into the aorta (Figure 8B). The maximum flow rate through the AV orifice is attained at $t_{hb} = 231$ ms, and it equals $Q_{max}^{AV} = 510$ ml/s, consistently with physiology.[143,150] It corresponds to an average velocity magnitude of $|\mathbf{u}|_{max}^{AV} = 1.46$ m/s on the AV section. The jet through the aortic valve is unsteady during all the ejection, consistently with the transitional nature of the flow (see Figure 8B). At the end of the ejection phase, the left ventricle attains its *end-systolic volume* ESV = 58.6 ml. Given EDV and ESV, we compute the *stroke volume* SV and *ejection fraction* EF as
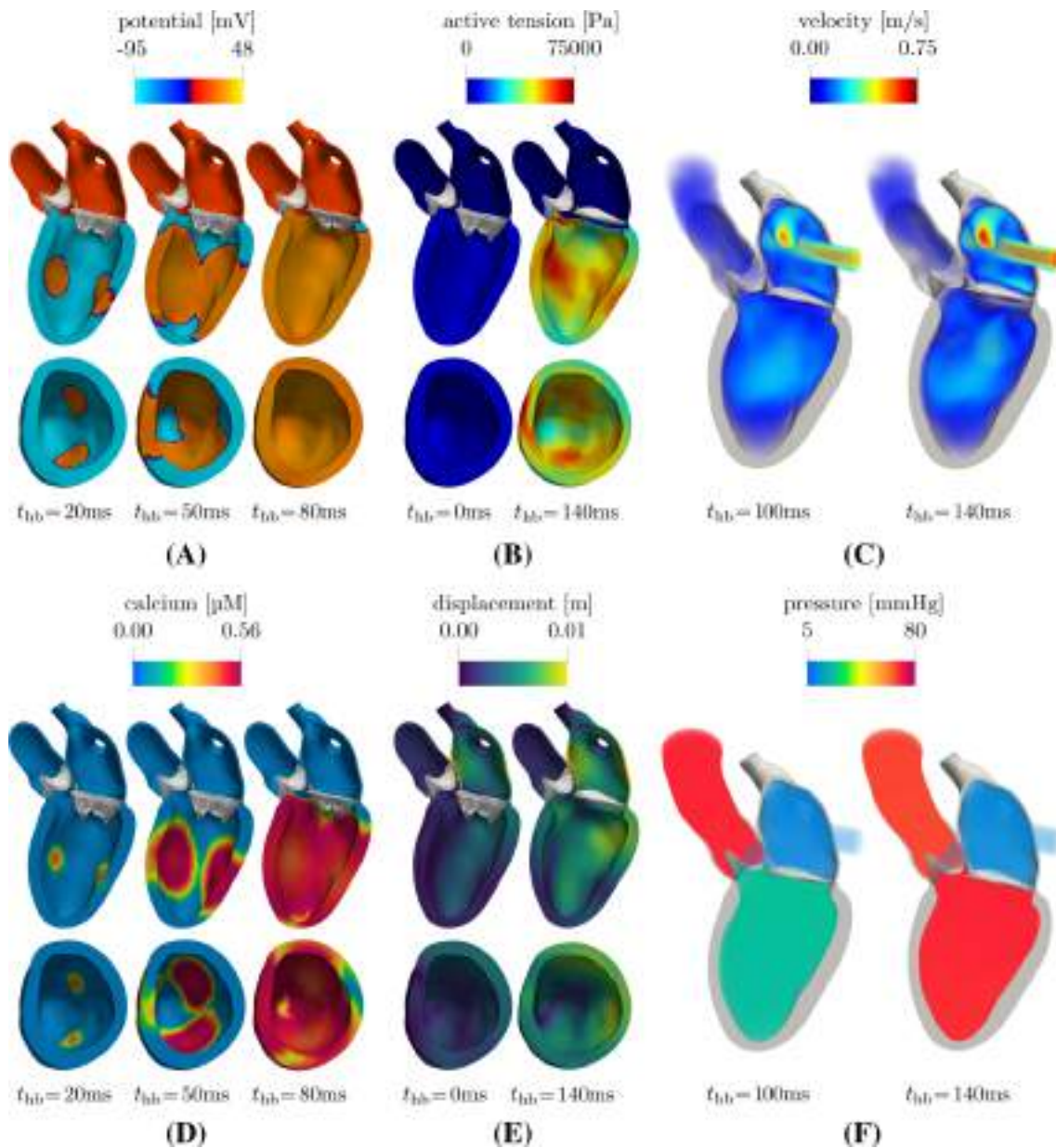
FIGURE 7 Solution snapshots during the isovolumetric contraction phase, as seen through a long-axis and a short-axis section: (A) transmembrane potential v; (B) active tension T_{act}; (C) volume rendering of the fluid velocity magnitude $|\mathbf{u}|$ (the opacity of the rendering is proportional to the magnitude); (D) intracellular calcium concentration $\left[\text{Ca}^{2+}\right]_i$; (E) displacement magnitude $|\mathbf{d}|$; (F) volume rendering of the fluid pressure p

$$\text{SV} = \text{EDV} - \text{ESV} = 80.4 \text{ ml} \quad \text{EF} = \frac{\text{SV}}{\text{EDV}} = 57.8 \% .$$

Both quantities are within normal physiological ranges (see Table 2).[140,141,149,151,152]

During the ejection phase, the ventricular pressure increases until $t_{\text{hb}} = 250$ ms, reaching a peak value of $p_{\text{max}}^{\text{LV}} = 126$ mmHg (see Figure 6), within the physiological ranges.[8,142] After that, pressure starts decreasing until it falls below the aortic pressure, at which point the AV starts closing.

A similar evolution characterizes the pressure in the ascending aorta, reported in Figure 9: starting from an end-diastolic value of 68 mmHg, it reaches a peak of 112 mmHg and then declines until the next heartbeat. Although the absolute pressure values are smaller than normal ones,[153] and there is a large pressure jump between the ventricle and the aorta (see Section 4), the time profile of the aortic pressure is remarkably similar to the ones obtained from in-vivo
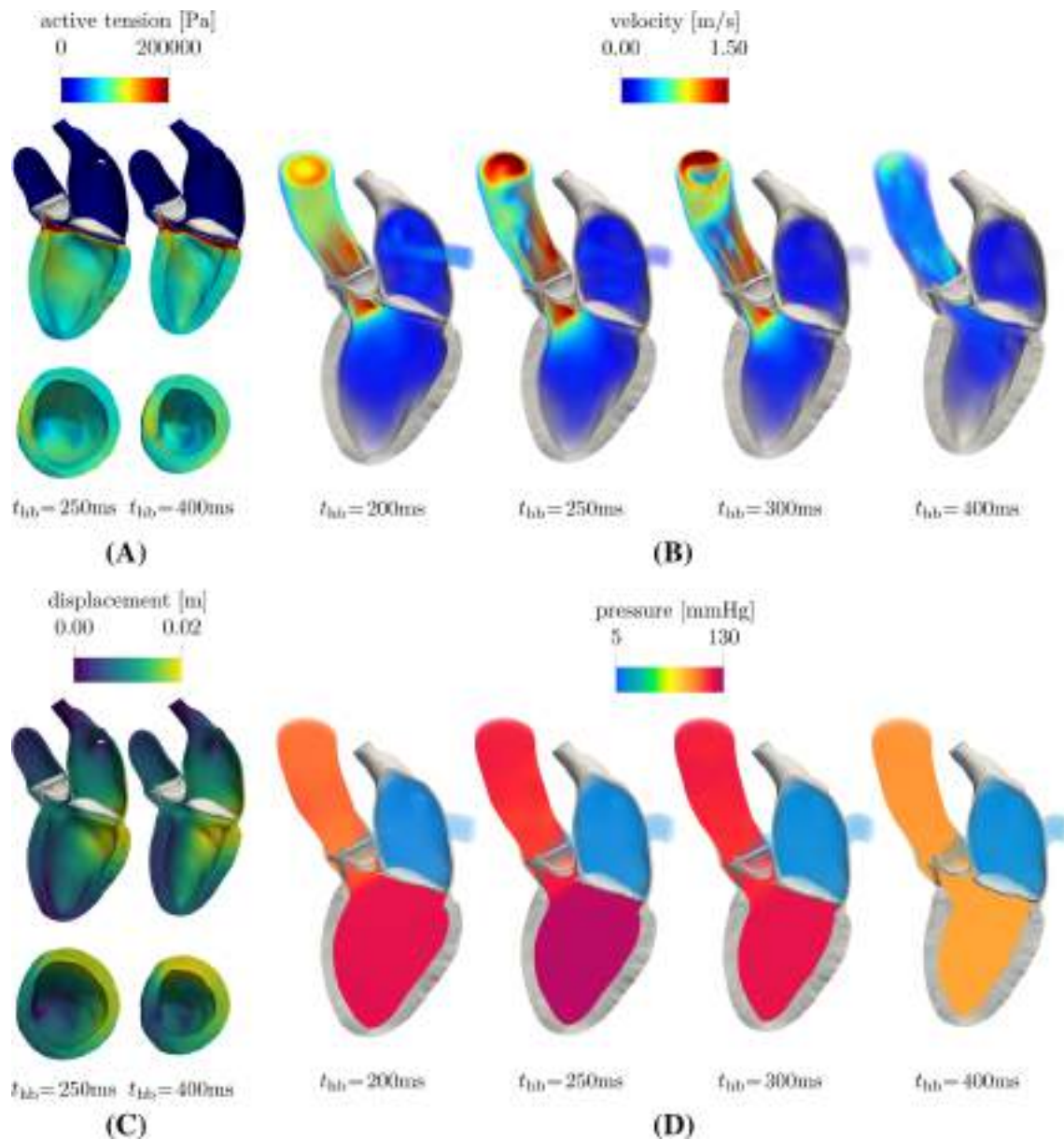
FIGURE 8 Solution snapshots during the ejection phase, as seen through a long-axis and a short-axis section: (A) active tension T_{act}; (B) volume rendering of the fluid velocity magnitude $|\mathbf{u}|$ (the opacity of the rendering is proportional to the magnitude); (C) displacement magnitude $|\mathbf{d}|$; (D) volume rendering of the fluid pressure p

measurements.[153,154] In particular, it features the *anacrotic notch*, resulting from the interaction of the forward and reflected pressure waves.[154] This effect is captured thanks to the FSI modeling framework, which, contrary to standalone CFD models, allows to obtain traveling pressure waves. The aortic pressure also features the *dicrotic notch*[8,152,153] in correspondence of the AV closure.

As the volume reduces, the ventricle becomes shorter and the atrioventricular plane shifts towards the ventricular apex (see Figure 10), as observed in healthy hearts.[8,27,155] We quantify this effect by computing the *longitudinal fractional shortening* (LFS)[27]: denoting by L_{ED} and L_{ES} the apico-basal distances at the end of diastole and at the end of systole, we have

$$\text{LFS} = \frac{L_{ED} - L_{ES}}{L_{ED}} = 17.8\ \% ,$$
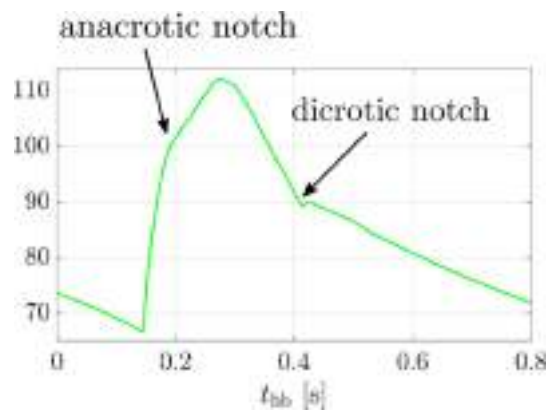
FIGURE 9 Average pressure in the ascending aorta over time. Notice the presence of the anacrotic notch during the systolic upstroke and of the dicrotic notch, or incisure, at the closing time of the aortic valve
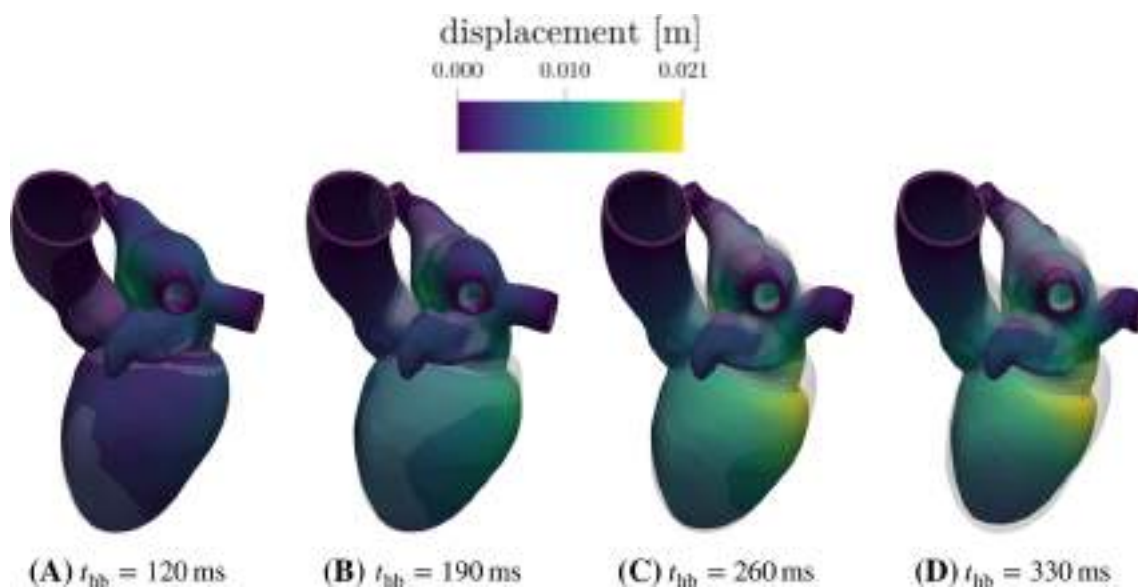

FIGURE 10 Magnitude of the displacement **d** at four instants during the ejection phase. The initial configuration is overlaid in trasparency, and the domain is warped by **d**. Notice how the ventricle becomes shorter during the ejection, mostly due to the shift of the atrioventricular plane towards the apex

which matches measurements on healthy hearts.[147] At the end of the systolic phase, the ventricular wall is approximately 14% thicker than at the end of diastole.[156]

During the late systolic phase, towards the end of the ejection, the ventricle repolarizes (Figure 11), with the transmembrane potential returning to its resting value.

Overall, the ejection phase lasts $T_{ej} = 261$ ms, and the whole systolic phase lasts $T_{sys} = 326$ ms, corresponding to 40.7% of the heartbeat.

3.3 | Isovolumetric relaxation

Once the AV is fully closed, the *isovolumetric relaxation* (IVR) phase starts (Figure 12). Ventricular pressure reduces as the ventricle relaxes at constant volume (Figure 6). This phase lasts for $T_{IVR} = 94.2$ ms, consistently with physiology,[145,146] and the MV starts opening as soon as the ventricular pressure becomes smaller than the atrial pressure.
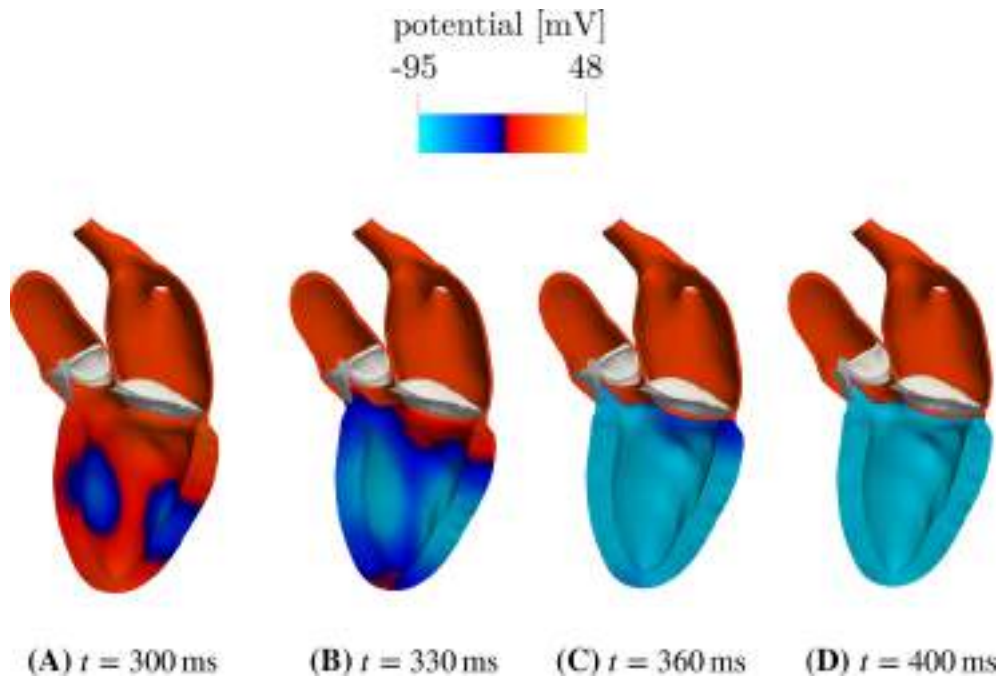
FIGURE 11 Repolarization of the left ventricle. The ventricular transmembrane potential gradually returns to its resting value

As observed for the IVC phase, our model features a small spurious variation in volume during isovolumetric phases. In the case of the IVR phase, the variation amounts to 0.4 ml, corresponding to 0.6% of the ESV. Also in this case, we deem the spurious variation to be acceptable.

3.4 | Filling

Once the MV is open, blood flows from the atrium into the ventricle (Figure 13B). The flow is characterized by the formation of a jet through the MV, that is associated to a vortex ring (Figure 14A). The vortex ultimately dissipates near to the ventricular free wall, while becoming larger near the septum (Figure 14B,C) resulting in a single vortex that rotates clockwise, if observed from a long-axis view with the septum on the left. This behavior is observed in medical images of healthy hearts.[157,158] At the same time, the atrioventricular plane shifts towards the atrium, while the ventricular volume increases. Since our model does not account for atrial contraction, the simulated diastolic phase lacks the atrial kick.[8] This also determines higher-than-normal pressure and volume in the left atrium (with a peak pressure of 19 mmHg, against a normal value of about 8 mmHg).[149] Filling continues until the ventricle starts contracting again, leading to the closure of the MV and the beginning of a new cardiac cycle. The filling phase lasts for $T_{\text{fil}} = 379$ ms, and the whole diastolic phase lasts for $T_{\text{dia}} = 474$ ms, corresponding to 59.3% of the heartbeat.

3.5 | Conservation of blood volume

The explicit treatment of the geometric FSI coupling condition and of the coupling between the Navier–Stokes equations and the circulation model might in principle lead to variations over time in the total blood volume. To assess whether this has an impact on simulation results, we compute the total blood volume over time as follows:

$$V_{\text{tot}}(t) = V_{\text{VEN}}^{\text{PUL}}(t) + V^{\text{LA}}(t) + V^{\text{LV}}(t) + V_{\text{AR}}^{\text{SYS}}(t) + V_{\text{VEN}}^{\text{SYS}}(t) + V_{\text{RA}}(t) + V_{\text{RV}}(t) + V_{\text{AR}}^{\text{PUL}}(t) ,$$

where $V^{\text{LA}}(t)$ and $V^{\text{LV}}(t)$ are the volumes of Ω^{LA} and $\Omega^{\text{LV}} \cup \Omega^{\text{ring}}$ at time t, respectively, and
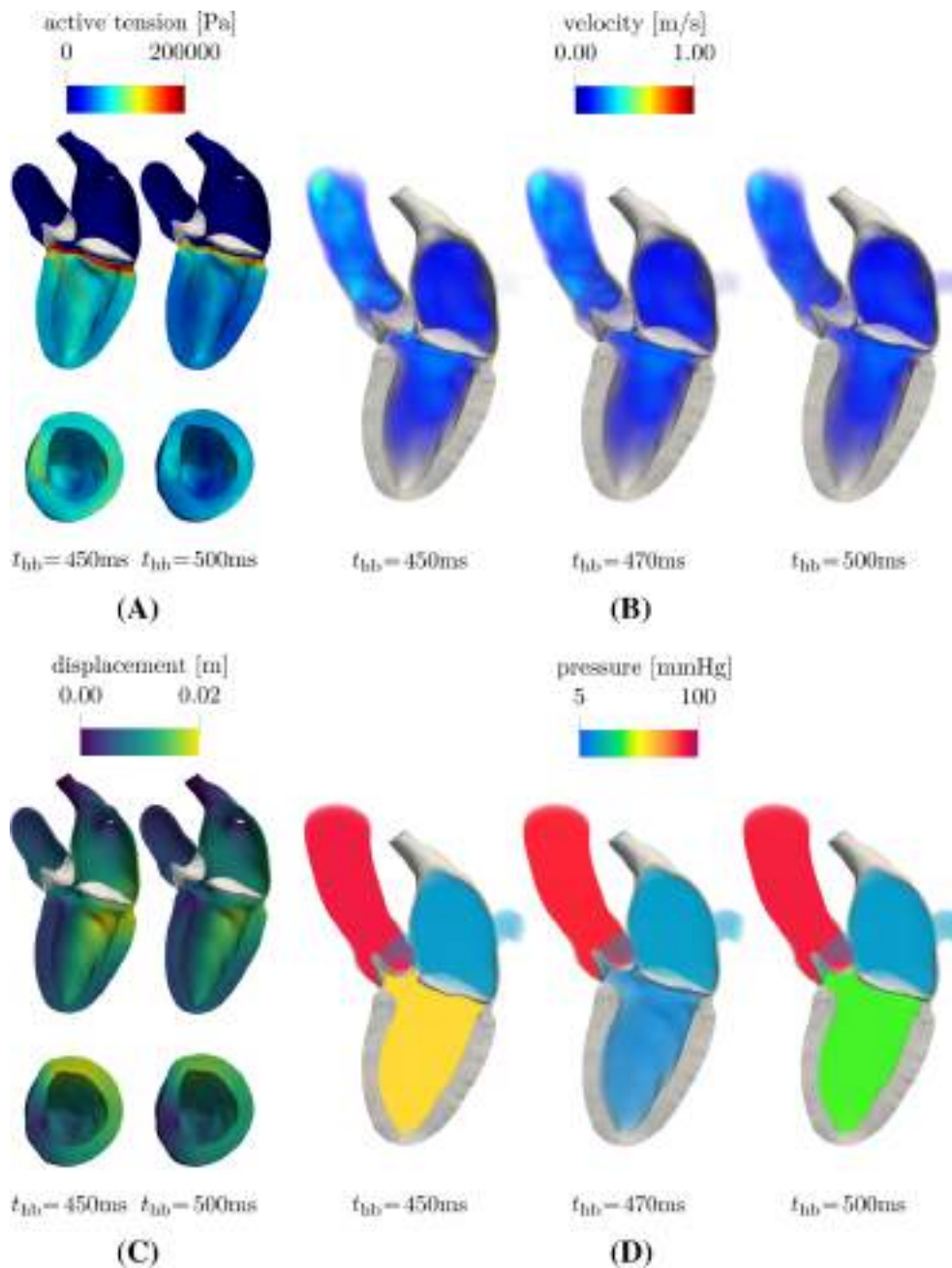
FIGURE 12 Solution snapshots during the isovolumetric relaxation phase, as seen through a long-axis and a short-axis section: (A) active tension T_{act}; (B) volume rendering of the fluid velocity magnitude $|\mathbf{u}|$ (the opacity of the rendering is proportional to the magnitude); (C) displacement magnitude $|\mathbf{d}|$; (D) volume rendering of the fluid pressure p

$$V_{\text{AR}}^{\text{SYS}}(t) = V_{\text{AR},0}^{\text{SYS}} + V^{\text{AA}}(t) + C_{\text{AR}}^{\text{SYS}}\left(p_{\text{AR}}^{\text{SYS}}(t) - p_{\text{EX}}(t)\right),$$

$$V_{\text{VEN}}^{\text{SYS}}(t) = V_{\text{VEN},0}^{\text{SYS}} + C_{\text{VEN}}^{\text{SYS}}\left(p_{\text{VEN}}^{\text{SYS}}(t) - p_{\text{EX}}(t)\right),$$

$$V_{\text{AR}}^{\text{PUL}}(t) = V_{\text{AR},0}^{\text{PUL}} + C_{\text{AR}}^{\text{PUL}}\left(p_{\text{AR}}^{\text{PUL}}(t) - p_{\text{EX}}(t)\right),$$

$$V_{\text{VEN}}^{\text{PUL}}(t) = V_{\text{VEN},0}^{\text{PUL}} + C_{\text{VEN}}^{\text{PUL}}\left(p_{\text{VEN}}^{\text{PUL}}(t) - p_{\text{EX}}(t)\right).$$

The latter equations are obtained by integrating the respective equations of the circulation model. We assume the zero-pressure volumes $V_{j,0}^{i}$ to be zero for simplicity, since they are constant in time and do not influence the assessment of blood volume conservation.
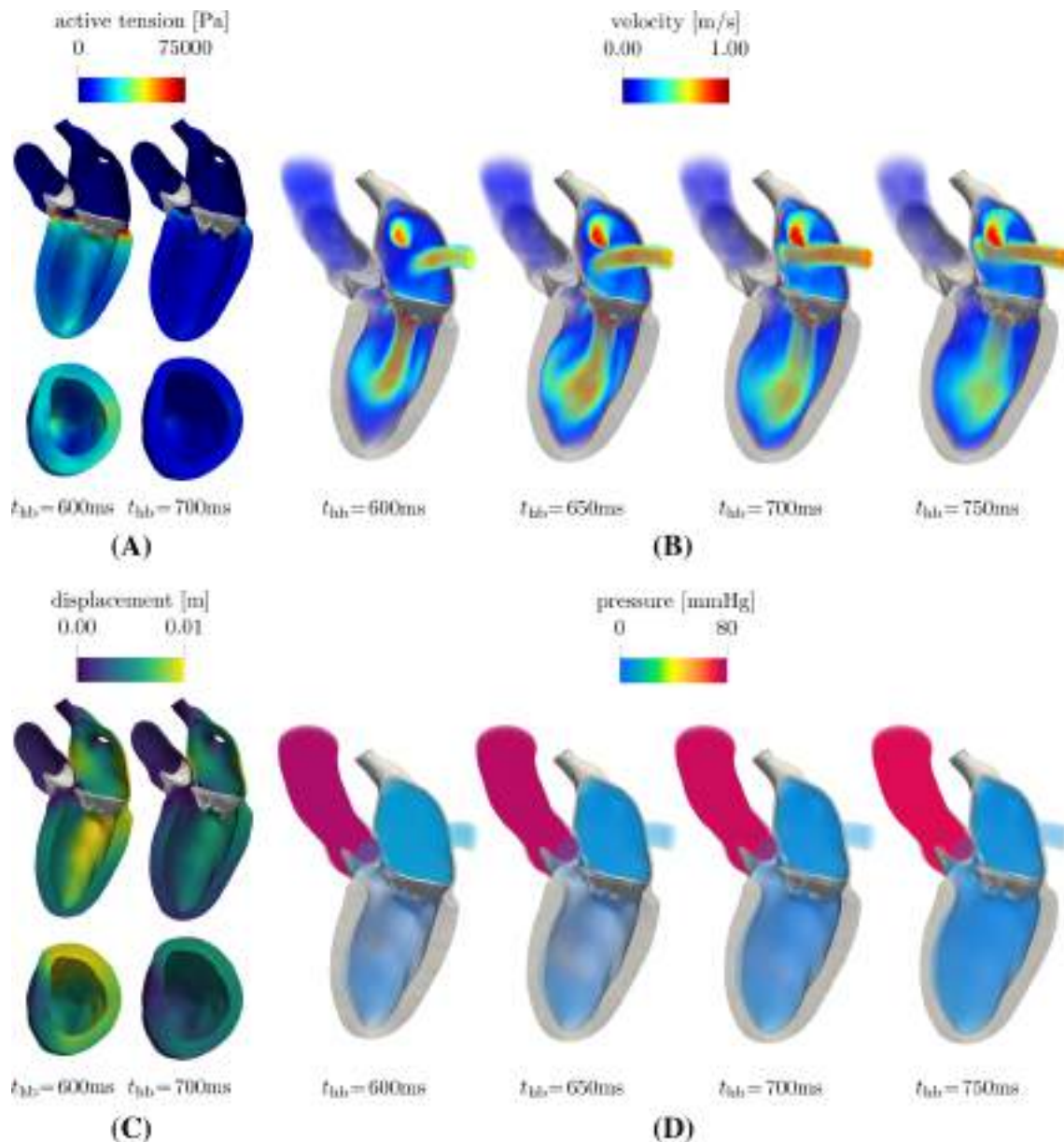
FIGURE 13   Solution snapshots during the filling phase, as seen through a long-axis and a short-axis section: (A) active tension T_{act}; (B) volume rendering of the fluid velocity magnitude $|\mathbf{u}|$ (the opacity of the rendering is proportional to the magnitude); (C) displacement magnitude $|\mathbf{d}|$; (D) volume rendering of the fluid pressure p

We report the blood volume over time for the different compartments, as well as the total blood volume, in Figure 15. From there, we can appreciate how the distribution of blood between the different compartments varies over time, but the total volume remains approximately constant. Indeed, the range of variation of the total volume over the three simulated heartbeats equals

$$\frac{\max_{t \in (0, \, T)} V_{tot}(t) - \max_{t \in (0, \, T)} V_{tot}(t)}{\max_{t \in (0, \, T)} V_{tot}(t)} = 0.0052 \, \% \, .$$

We deem this very small variation over three heartbeats to be negligible and the result highly accurate. Therefore, the approximation introduced by the explicit discretization of geometric FSI coupling and circulation coupling does not introduce significant errors in terms of mass conservation.
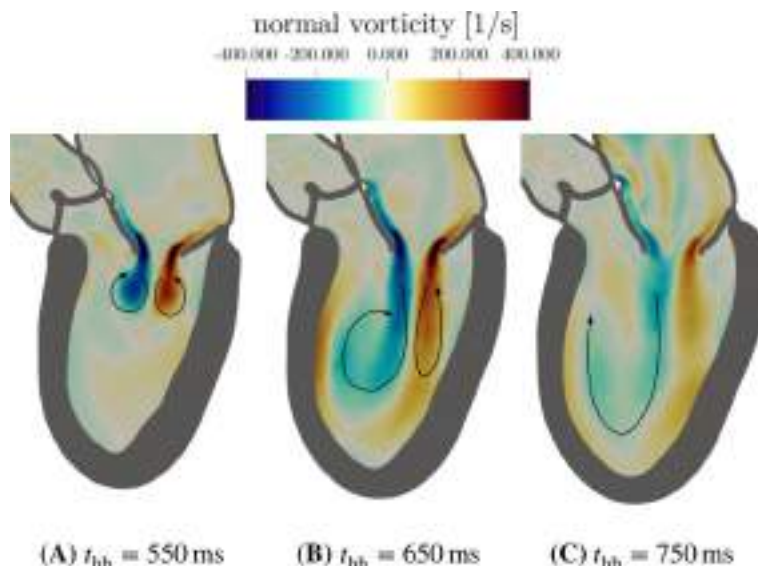
FIGURE 14 Vorticity $\mathbf{w} \times \mathbf{N} = (\mathbf{u}) \times \mathbf{N}$ of the velocity field, projected onto a slice of the domain (with normal $\mathbf{N}$ pointing outwards from the slice plane). The arrows indicate the direction of the rotating vortices
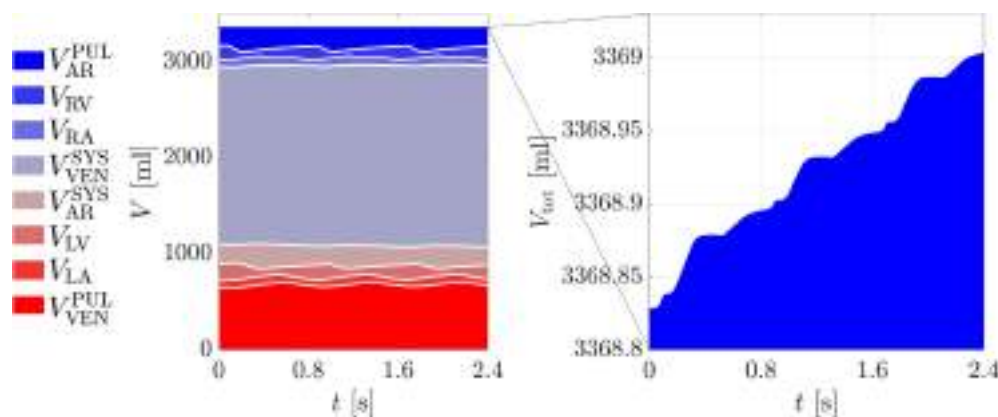

FIGURE 15 Blood volume over three heartbeats in each compartment of the heart and circulation. The zoom on the right shows how the total blood volume exhibits a very small variation in time: the mass gain over three heartbeats is only 0.0052% of the total

4 | LIMITATIONS OF THE CURRENT STUDY

In this section we present some limitations associated to the proposed computational framework, related to modeling choices and simplifications. To begin with, we modeled the LA as passive from both the electrical and mechanical viewpoints, for simplicity. Doing so, we do not need to surrogate the presence of the atrium by means of boundary conditions for ventricular mechanics.[12] However, in real hearts, the left atrium is electrically active and contracts at the end of the diastolic phase, providing extra preload to the left ventricle along with an additional jet through the MV.[8,9] Our model does not capture these features. However, the proposed model serves as a milestone towards the development of a four-chamber EMF model. The 3D inclusion of the atrium, albeit in a simplified way, is instrumental towards this goal. Moreover, our geometrical model only includes the left portion of the heart, although there is a significant interaction between the left and right sides. The development of a model including atrial electromechanics and the whole heart will be the subject of future studies.

The stimulation protocol used to trigger the activation of the myocardium is simplified if compared to the behavior of the cardiac conduction system.[8,15,18,20,86,87] While this simplification is acceptable in physiological conditions,[30] more detailed models might yield better descriptions of the ventricular activation pattern, which can become especially relevant if pathological scenarios are considered. A more realistic representation of the conduction system can be achieved,

for instance, by including a fast conducting endocardial layer,[159] a denser network of stimuli[18,20,87] or a multiscale model of the cardiac conduction system.[15] Moreover, we do not include in our model stretch-activated currents or other mechano-electric feedback effects besides the geometry-mediated ones. Pericardium boundary conditions are assumed homogeneous in space, for simplicity: introducing spatial variability in their coefficients may allow to improve the numerical results.[28,32]

We employed the RIIS model for valve dynamics, prescribing the kinematics of the valve and neglecting any dynamic interaction with the blood. Moreover, we displace the valves along with the fluid domain displacement $\mathbf{d}_{ALE}$, which has no physical meaning. Valve FSI plays a major role in the blood dynamics,[45,46,111,114,115,117,160] as well as being responsible for several pathologies of clinical interest.[35,113] While in this work we are mostly interested on the macroscopic effect of valves on the blood flow, the incorporation of suitable FSI models of the valves will be the subject of future studies.

In terms of numerical results, one major mismatch between our model and physiological data is the pressure difference between the ventricle and the aorta during the ejection phase. We obtain a maximum pressure difference of 18 mmHg. Such a high value, although not uncommon in the cardiac modeling literature,[40,59] is typically associated with a stenotic valve in clinical measurements.[161,162] The high pressure jump in our numerical results is also related to an aortic pressure that is smaller than what is normally observed.[153] We believe this to be caused by minor inconsistencies in the geometrical model (based on a template obtained averaging over a sample of people, rather than on a specific individual) and by the simplicity of the valve model considered. In any case, further investigations on this point are in order.

Finally, we compared our results against normal ranges for healthy individuals, since the geometrical model represents an average heart. An alternative, more individualized approach, not explored in this work, is based on the calibration of the model to replicate measurements on a single patient. This has the potential of providing more insight on the ability of the model to reproduce the physics of the heart, as well as paving the way for potential clinical applications. This patient-specific validation, supported by algorithms for data assimilation, is a fundamental step towards the construction of a heart digital twin.

5 | CONCLUSIONS

We introduced a novel fully integrated computational framework for the modeling and simulation of the human heart. The proposed model features three-dimensional and highly detailed descriptions of electrophysiology, active and passive mechanics and blood dynamics, as well as reduced models for valves and circulation. We included feedback effects among the different core models, resulting in a coupled multiphysics and multiscale problem.

Suitable numerical techniques were presented with the aim of solving efficiently the model equations. In particular, a staggered scheme with respect to time allowed for a flexible and efficient solution. Numerical methods were implemented in a high-performance computing framework within the lifex library. We simulated a human left heart, and the results indicate that the proposed computational framework has the potential of describing accurately the physics of the heart, accounting for multiple feedback effects and overall capturing the interplay between the different processes driving the heartbeat. Our model is capable of representing all phases of the heartbeat and their durations, in accordance with clinical data. Moreover, through the coupling with a closed-loop circulation model, we were able to account for the interplay between the heart and the circulatory system, and guarantee the total blood volume conservation in time. The model correctly represents isovolumetric phases of the heartbeat, and reproduces effects associated to traveling pressure waves, thanks to the FSI coupling, suggesting that an EMF coupled modeling framework can overcome some of the limitations of electromechanics-driven CFD simulations. A more systematic comparison of the two modeling approaches will be the subject of future studies.

The agreement between numerical results and biomarkers from the medical literature suggests that the proposed model can be used for the investigation of the physiological cardiac function as well as for the simulation of pathological scenarios, and can serve as a stepping stone towards realistic and accurate integrated models of the whole heart.

DATA AVAILABILITY STATEMENT
Data sharing is not applicable to this article as no new data were created or analyzed in this study.

ORCID
Michele Bucelli https://orcid.org/0000-0003-3089-9734
Alberto Zingaro https://orcid.org/0000-0002-1522-9647
Pasquale Claudio Africa https://orcid.org/0000-0002-0706-8564
Ivan Fumagalli https://orcid.org/0000-0001-9256-1398
Luca Dede' https://orcid.org/0000-0002-6558-8277
Alfio Quarteroni https://orcid.org/0000-0002-5947-6885

ENDNOTE
i See https://wiki.u-gov.it/confluence/display/SCAIUS/UG3.3%3A+GALILEO100+UserGuide for technical specifications.

REFERENCES

1. Benjamin EJ, Blaha MJ, Chiuve SE, et al. Heart disease and stroke statistics—2017 update: a report from the American Heart Association. *Circulation*. 2017;135(10):e146-e603. doi:10.1161/CIR.0000000000000485

2. Gerach T, Schuler S, Fröhlich J, et al. Electro-mechanical whole-heart digital twins: a fully coupled multi-physics approach. *Mathematics*. 2021;9(11):1247. doi:10.3390/math9111247

3. Gray RA, Pathmanathan P. Patient-specific cardiovascular computational modeling: diversity of personalization and challenges. *J Cardiovasc Transl Res*. 2018;11(2):80-88. doi:10.1007/s12265-018-9792-2

4. Karabelas E, Longobardi S, Fuchsberger J, et al. Global sensitivity analysis of four chamber heart hemodynamics using surrogate models. *IEEE Trans Biomed Eng*. 2022;69(10):3216-3223. doi:10.1109/TBME.2022.3163428

5. Niederer SA, Lumens J, Trayanova NA. Computational models in cardiology. *Nat Rev Cardiol*. 2019;16(2):100-111. doi:10.1038/s41569-018-0104-y

6. Quarteroni A, Lassila T, Rossi S, Ruiz-Baier R. Integrated heart—coupling multiscale and multiphysics models for the simulation of the cardiac function. *Comput Methods Appl Mech Eng*. 2017;314:345-407. doi:10.1016/j.cma.2016.05.031

7. Quarteroni A, Dede' L, Manzoni A, Vergara C. *Mathematical Modelling of the Human Cardiovascular System: Data, Numerical Approximation, Clinical Applications*. Cambridge University Press; 2019.

8. Katz AM. *Physiology of the Heart*. Lippincott Williams & Wilkins; 2010.

9. Klabunde R. *Cardiovascular Physiology Concepts*. Lippincott Williams & Wilkins; 2011.

10. Hosoi A, Washio T, Ji O, Kadooka Y, Nakajima K, Hisada T. A multi-scale heart simulation on massively parallel computers. *Proceedings of the 2010 ACM/IEEE International Conference for High Performance Computing, Networking, Storage and Analysis*. 2010;1-11.

11. Ji O, Washio T, Sugiura S, Hisada T. Clinical and pharmacological application of multiscale multiphysics heart simulator, UT-heart. *Korean J Physiol Pharmacol*. 2019;23(5):295-303. doi:10.4196/kjpp.2019.23.5.295

12. Santiago A, Aguado-Sierra J, Zavala-Aké M, et al. Fully coupled fluid-electro-mechanical model of the human heart for supercomputers. *Int J Numer Methods Biomed Eng*. 2018;34(12):e3140. doi:10.1002/cnm.3140

13. Arevalo HJ, Vadakkumpadan F, Guallar E, et al. Arrhythmia risk stratification of patients after myocardial infarction using personalized heart models. *Nat Commun*. 2016;7(1):1-8. doi:10.1038/ncomms11437

14. Bucelli M, Salvador M, Dede' L, Quarteroni A. Multipatch isogeometric analysis for electrophysiology: simulation in a human heart. *Comput Methods Appl Mech Eng*. 2021;376:113666. doi:10.1016/j.cma.2021.113666

15. Del Corso G, Verzicco R, Viola F. A fast computational model for the electrophysiology of the whole human heart. *J Comput Phys*. 2022;457:111084. doi:10.1016/j.jcp.2022.111084

16. Gillette K, Gsell MA, Prassl AJ, et al. A framework for the generation of digital twins of cardiac electrophysiology from clinical 12-leads ECGs. *Med Image Anal*. 2021;71:102080. doi:10.1016/j.media.2021.102080

17. Piersanti R, Africa PC, Fedele M, et al. Modeling cardiac muscle fibers in ventricular and atrial electrophysiology simulations. *Comput Methods Appl Mech Eng*. 2021;373:113468. doi:10.1016/j.cma.2020.113468

18. Romero D, Sebastian R, Bijnens BH, et al. Effects of the Purkinje system and cardiac geometry on biventricular pacing: a model study. *Ann Biomed Eng*. 2010;38(4):1388-1398. doi:10.1007/s10439-010-9926-4

19. Trayanova NA. Whole-heart modeling: applications to cardiac electrophysiology and electromechanics. *Circ Res*. 2011;108(1):113-128. doi:10.1161/CIRCRESAHA.110.223610

20. Vergara C, Lange M, Palamara S, Lassila T, Frangi AF, Quarteroni A. A coupled 3D–1D numerical monodomain solver for cardiac electrical activation in the myocardium with detailed Purkinje network. *J Comput Phys*. 2016;308:218-238. doi:10.1016/j.jcp.2015.12.016

21. Augustin CM, Crozier A, Neic A, et al. Patient-specific modeling of left ventricular electromechanics as a driver for haemodynamic analysis. *EP Europace*. 2016;18:iv121-iv129. doi:10.1093/europace/euw369

22. Baillargeon B, Rebelo N, Fox DD, Taylor RL, Kuhl E. The living heart project: a robust and integrative simulator for human heart function. *Eur J Mech: A/Solids*. 2014;48:38-47. doi:10.1016/j.euromechsol.2014.04.001

23. Dede' L, Gerbi A, Quarteroni A. *Segregated algorithms for the numerical simulation of cardiac electromechanics in the left human ventricle*. Springer; 2020:81-116.

24. Fedele M, Piersanti R, Regazzoni F, et al. A comprehensive and biophysically detailed computational model of the whole human heart electromechanics. *arXiv Preprint arXiv:2207.12460* 2022. doi: 10.48550/arXiv.2207.12460

25. Gerbi A, Dede' L, Quarteroni A. A monolithic algorithm for the simulation of cardiac electromechanics in the human left ventricle. *Math Eng*. 2019;1(1):1-37. doi:10.3934/Mine.2018.1.1

26. Gurev V, Lee T, Constantino J, Arevalo H, Trayanova NA. Models of cardiac electromechanics based on individual hearts imaging data: image-based electromechanical models of the heart. *Biomech Model Mechanobiol*. 2011;10(3):295-306. doi:10.1007/s10237-010-0235-5

27. Levrero-Florencio F, Margara F, Zacur E, et al. Sensitivity analysis of a strongly-coupled human-based electromechanical cardiac model: effect of mechanical parameters on physiologically relevant biomarkers. *Comput Methods Appl Mech Eng*. 2020;361:112762. doi:10.1016/j.cma.2019.112762

28. Pfaller MR, Hörmann JM, Weigl M, et al. The importance of the pericardium for cardiac biomechanics: from physiology to computational modeling. *Biomech Model Mechanobiol*. 2019;18(2):503-529. doi:10.1007/s00791-002-0081-9

29. Piersanti R, Regazzoni F, Salvador M, et al. 3D–0D closed-loop model for the simulation of cardiac biventricular electromechanics. *Comput Methods Appl Mech Eng*. 2022;391:114607. doi:10.1016/j.cma.2022.114607

30. Regazzoni F, Salvador M, Africa PC, Fedele M, Dede L, Quarteroni A. A cardiac electromechanical model coupled with a lumped-parameter model for closed-loop blood circulation. *J Comput Phys*. 2022;457:111083. doi:10.1016/j.jcp.2022.111083

31. Salvador M, Fedele M, Africa PC, et al. Electromechanical modeling of human ventricles with ischemic cardiomyopathy: numerical simulations in sinus rhythm and under arrhythmia. *Comput Biol Med*. 2021;136:104674. doi:10.1016/j.compbiomed.2021.104674

32. Strocchi M, Gsell MA, Augustin CM, et al. Simulating ventricular systolic motion in a four-chamber heart model with spatially varying Robin boundary conditions to model the effect of the pericardium. *J Biomech*. 2020;101:109645. doi:10.1016/j.jbiomech.2020.109645

33. Usyk TP, LeGrice IJ, McCulloch AD. Computational model of three-dimensional cardiac electromechanics. *Comput Vis Sci*. 2002;4(4):249-257. doi:10.1007/s00791-002-0081-9

34. Chnafa C, Mendez S, Nicoud F. Image-based large-eddy simulation in a realistic left heart. *Comput Fluids*. 2014;94:173-187. doi:10.1016/j.compfluid.2014.01.030

35. Collia D, Zovatto L, Pedrizzetti G. Analysis of mitral valve regurgitation by computational fluid dynamics. *APL Bioeng*. 2019;3(3):036105. doi:10.1063/1.5097245

36. Kronborg J, Svelander F, Eriksson-Lidbrink S, et al. Computational analysis of flow structures in turbulent ventricular blood flow associated with mitral valve intervention. *Front Physiol*. 2022;13:752. doi:10.3389/fphys.2022.806534

37. Rigatelli G, Chiastra C, Pennati G, Dubini G, Migliavacca F, Zuin M. Applications of computational fluid dynamics to congenital heart diseases: a practical review for cardiovascular professionals. *Expert Rev Cardiovasc Ther*. 2021;19(10):907-916. doi:10.1080/14779072.2021.1999229

38. Spühler JH, Jansson J, Jansson N, Hoffman J. *A High Performance Computing Framework for Finite Element Simulation of Blood Flow in the Left Ventricle of the Human Heart*. Springer; 2020:155-164.

39. Terahara T, Kuraishi T, Takizawa K, Tezduyar TE. Computational flow analysis with boundary layer and contact representation: II. Heart valve flow with leaflet contact. *J Mech*. 2022;38:185-194. doi:10.1093/jom/ufac013

40. This A, Boilevin-Kayl L, Fernández MA, Gerbeau JF. Augmented resistive immersed surfaces valve model for the simulation of cardiac hemodynamics with isovolumetric phases. *Int J Numer Methods Biomed Eng*. 2020;36(3):e3223. doi:10.1002/cnm.3223

41. VedulaV SJH, LardoAC MR. Effect of trabeculae and papillary muscles on the hemodynamics of the left ventricle. *Theor Comput Fluid Dyn*. 2016;30(1):3-21. doi:10.1007/s00162-015-0349-6

42. Zingaro A, Dede' L, Menghini F, Quarteroni A. Hemodynamics of the heart's left atrium based on aVariational multiscale-LES numerical method. *Eur J Mech: B/Fluids*. 2021;89:380-400. doi:10.1016/j.euromechflu.2021.06.014

43. Zingaro A, Fumagalli I, Dede' L, et al. A geometric multiscale model for the numerical simulation of blood flow in the human left heart. *Discr Contin Dyn Syst-S*. 2022;15(8):2391-2427. doi:10.3934/dcdss.2022052

44. Cheng Y, Oertel H, Schenkel T. Fluid-structure coupled CFD simulation of the left ventricular flow during filling phase. *Ann Biomed Eng*. 2005;33(5):567-576. doi:10.1007/s10439-005-4388-9

45. Einstein DR, Del Pin F, Jiao X, et al. Fluid–structure interactions of the mitral valve and left heart: comprehensive strategies, past, present and future. *Int J Numer Methods Biomed Eng*. 2010;26(3–4):348-380. doi:10.1002/cnm.1280

46. Feng L, Gao H, Griffith B, Niederer S, Luo X. Analysis of a coupled fluid-structure interaction model of the left atrium and mitral valve. *Int J Numer Methods Biomed Eng*. 2019;35(11):e3254. doi:10.1002/cnm.3254

47. Gao H, Feng L, Qi N, Berry C, Griffith BE, Luo X. A coupled mitral valve–left ventricle model with fluid–structure interaction. *Med Eng Phys*. 2017;47:128-136. doi:10.1016/j.medengphy.2017.06.042

48. Hirschhorn M, Tchantchaleishvili V, Stevens R, Rossano J, Throckmorton A. Fluid–structure interaction modeling in cardiovascular medicine—A systematic review 2017–2019. *Med Eng Phys*. 2020;78:1-13. doi:10.1016/j.medengphy.2020.01.008

49. Brenneisen J, Daub A, Gerach T, et al. Sequential coupling shows minor effects of fluid dynamics on myocardial deformation in a realistic whole-heart model. *Front Cardiovasc Med*. 2021;8:1-13. doi:10.3389/fcvm.2021.768548

50. Khodaei S, Henstock A, Sadeghi R, et al. Personalized intervention cardiology with transcatheter aortic valve replacement made possible with a non-invasive monitoring and diagnostic framework. *Sci Rep*. 2021;11(1):1-28. doi:10.1038/s41598-021-85500-2

51. Nordsletten D, McCormick M, Kilner P, Hunter P, Kay D, Smith N. Fluid–solid coupling for the investigation of diastolic and systolic human left ventricular function. *Int J Numer Methods Biomed Eng*. 2011;27(7):1017-1039. doi:10.1002/cnm.1405

52. Zhang Q, Hisada T. Analysis of fluid–structure interaction problems with structural buckling and large domain changes by ALE finite element method. *Comput Methods Appl Mech Eng*. 2001;190(48):6341-6357. doi:10.1016/S0045-7825(01)00231-6

53. Bucelli M, Gabriel MG, Gigante G, Quarteroni A, Vergara C. A stable loosely-coupled scheme for cardiac electro-fluidstructure interaction. arXiv preprint arXiv:2210.00917 2022.

54. Gerbi A. *Numerical approximation of cardiac electro-fluid-mechanical models*. PhD thesis EPFL, Lausanne, Switzerland; 2018.

55. Sugiura S, Okada JI, Washio T, Hisada T. *UT-Heart: A Finite Element Model Designed for the Multiscale and Multiphysics Integration of our Knowledge on the Human Heart*. Springer; 2022:221-245.

56. Verzicco R. Electro-fluid-mechanics of the heart. *J Fluid Mech*. 2022;941:941. doi:10.1017/jfm.2022.272

57. Kariya T, Washio T, Ji O, et al. Personalized perioperative multi-scale, multi-physics heart simulation of double outlet right ventricle. *Ann Biomed Eng*. 2020;48(6):1740-1750. doi:10.1007/s10439-020-02488-y

58. Bakir AA, Al Abed A, Stevens MC, Lovell NH, Dokos S. A multiphysics biventricular cardiac model: simulations with a left-ventricular assist device. *Front Physiol*. 2018;9:1259.

59. Viola F, Meschini V, Verzicco R. Fluid–structure–electrophysiology interaction (FSEI) in the left-heart: a multi-way coupled computational model. *Eur J Mech: B/Fluids*. 2020;79:212-232. doi:10.1016/j.euromechflu.2019.09.006

60. Viola F, Meschini V, Verzicco R. Effects of stenotic aortic valve on the left heart hemodynamics: A fluid-structureelectrophysiology approach. *arXiv Preprint arXiv:2103.14680*, 2021. doi: 10.48550/arXiv.2103.14680

61. Nash MP, Panfilov AV. Electromechanical model of excitable tissue to study reentrant cardiac arrhythmias. *Prog Biophys Mol Biol*. 2004;85(2–3):501-522. doi:10.1016/j.pbiomolbio.2004.01.016

62. Viola F, Spandan V, Meschini V, et al. FSEI-GPU: GPU accelerated simulations of the fluid–structure–electrophysiology interaction in the left heart. *Comput Phys Commun*. 2022;273:108248. doi:10.1016/j.cpc.2021.108248

63. Viola F, Del Corso G, De Paulis R, Verzicco R. GPU accelerated digital twins of the human heart open new routes for cardiovascular research. Research Square Preprint 2022.

64. Battista NA, Miller LA. Bifurcations in valveless pumping techniques from a coupled fluid-structure-electrophysiology model in heart development. *Biomath*. 2017;6(2):ID–1711297. doi:10.11145/j.biomath.2017.11.297

65. Salvador M, Regazzoni F, Pagani S, Trayanova N, Quarteroni A. The role of mechano-electric feedbacks and hemodynamic coupling in scar-related ventricular tachycardia. *Comput Biol Med*. 2022;142:105203. doi:10.1016/j.compbiomed.2021.105203

66. Regazzoni F, Dede′ L, Quarteroni A. Biophysically detailed mathematical models of multiscale cardiac active mechanics. *PLoS Comput Biol*. 2020;16(10):e1008294. doi:10.1371/journal.pcbi.1008294

67. Bucelli M, Dede′ L, Quarteroni A, Vergara C. Partitioned and monolithic FSI schemes for the numerical simulation of the heart. *Commun Comput Phys*. 2022.

68. Hirschvogel M, Bassilious M, Jagschies L, Wildhirt SM, Gee MW. A monolithic 3D-0D coupled closed-loop model of the heart and the vascular system: experiment-based parameter estimation for patient-specific cardiac mechanics. *Int J Numer Methods Biomed Eng*. 2017;33(8):e2842. doi:10.1002/cnm.2842

69. Zingaro A, Bucelli M, Fumagalli I, Dede′ L, Quarteroni A. Modeling isovolumetric phases in cardiac flows by an augmented resistive immersed implicit surface method. *arXiv Preprint arXiv:2208.09435*, 2022. doi: 10.48550/arXiv.2208.09435

70. Hughes TJ. *The Finite Element Method: Linear Static and Dynamic Finite Element Analysis*. Courier Corporation; 2012.

71. Quarteroni A. *Numerical Models for Differential Problems*. Springer; 2017.

72. Africa PC. Lifex: a flexible, high performance library for the numerical solution of complex finite element problems. *arXiv Preprint arXiv:2207.14668* 2022. doi: 10.48550/arXiv.2207.14668

73. Africa PC, Piersanti R, Fedele M, Dede′ L, Quarteroni A. Lifex–heart module: a high-performance simulator for the cardiac function package 1: fiber generation. *arXiv Preprint arXiv:2201.03303* 2022. doi: 10.48550/arXiv.2201.03303

74. Official lifex website. Accessed: October 4, 2022. https://lifex.gitlab.io/.

75. Roberts DE, Hersh LT, Scher AM. Influence of cardiac fiber orientation on wavefront voltage, conduction velocity, and tissue resistivity in the dog. *Circ Res*. 1979;44(5):701-712. doi:10.1161/01.RES.44.5.701

76. Eriksson TS, Prassl AJ, Plank G, Holzapfel GA. Influence of myocardial fiber/sheet orientations on left ventricular mechanical contraction. *Math Mech Solids*. 2013;18(6):592-606. doi:10.1177/1081286513485779

77. Gil D, Aris R, Borras A, Ramírez E, Sebastian R, Vazquez M. Influence of fiber connectivity in simulations of cardiac biomechanics. *Int J Comput Assist Radiol Surg*. 2019;14(1):63-72. doi:10.1007/s11548-018-1849-9

78. Doste R, Soto-Iglesias D, Bernardino G, et al. A rule-based method to model myocardial fiber orientation in cardiac biventricular geometries with outflow tracts. *Int J Numer Methods Biomed Eng*. 2019;35(4):e3185. doi:10.1002/cnm.3185

79. Rossi S, Lassila T, Ruiz-Baier R, Sequeira A, Quarteroni A. Thermodynamically consistent orthotropic activation model capturing ventricular systolic wall thickening in cardiac electromechanics. *Eur J Mech: A/Solids*. 2014;48:129-142. doi:10.1016/j.euromechsol.2013.10.009

80. Bayer JD, Blake RC, Plank G, Trayanova NA. A novel rule-based algorithm for assigning myocardial fiber orientation to computational heart models. *Ann Biomed Eng*. 2012;40(10):2243-2254. doi:10.1007/s10439-012-0593-5

81. Colli Franzone P, Pavarino LF, Scacchi S. *Mathematical Cardiac Electrophysiology*. Springer; 2014.

82. Sundnes J, Lines GT, Cai X, Nielsen BF, Mardal KA, Tveito A. *Computing the Electrical Activity in the Heart*. Springer Science & Business Media; 2007.

83. Ten Tusscher KH, Panfilov AV. Alternans and spiral breakup in a human ventricular tissue model. *Am J Phys Heart Circ Phys*. 2006; 291(3):H1088-H1100. doi:10.1152/ajpheart.00109.2006

84. Collet A. Numerical Modeling of the Cardiac Mechano-Electric Feedback within a Thermo-Electro-Mechanical Framework. Study of its Consequences on Arrhythmogenesis. PhD thesis. Université de Liège, Liège, Belgique; 2015.

85. Timmermann V, Dejgaard LA, Haugaa KH, et al. An integrative appraisal of mechano-electric feedback mechanisms in the heart. *Prog Biophys Mol Biol*. 2017;130:404-417.

86. Costabal FS, Hurtado DE, Kuhl E. Generating Purkinje networks in the human heart. *J Biomech*. 2016;49(12):2455-2465. doi:10.1016/j.jbiomech.2015.12.025

87. Landajuela M, Vergara C, Gerbi A, Dede' L, Formaggia L, Quarteroni A. Numerical approximation of the electromechanical coupling in the left ventricle with inclusion of the Purkinje network. *Int J Numer Methods Biomed Eng*. 2018;34(7):e2984. doi:10.1002/cnm.2984

88. Jacob R, Dierberger B, Kissling G. Functional significance of the frank-Starling mechanism under physiological and pathophysiological conditions. *Eur Heart J*. 1992;13(suppl_E):7-14. doi:10.1093/eurheartj/13.suppl_E.7

89. Opie LH. *Heart Physiology: From Cell to Circulation*. Lippincott Williams & Wilkins; 2004.

90. Bers D. *Excitation-Contraction Coupling and Cardiac Contractile Force*. Springer Science & Business Media; 2001.

91. Regazzoni F, Quarteroni A. An oscillation-free fully staggered algorithm for velocity-dependent active models of cardiac mechanics. *Comput Methods Appl Mech Eng*. 2021;373:113506. doi:10.1016/j.cma.2020.113506

92. Ogden R. *Non-Linear Elastic Deformations*. Courier Corporation; 2013.

93. Ambrosi D, Pezzuto S. Active stress vs. active strain in mechanobiology: constitutive issues. *J Elast*. 2012;107(2):199-212. doi:10.1007/s10659-011-9351-4

94. Göktepe S, Kuhl E. Electromechanics of the heart: a unified approach to the strongly coupled excitation–contraction problem. *Comput Mech*. 2010;45(2):227-243. doi:10.1007/s00466-009-0434-z

95. Pathmanathan P, Chapman S, Gavaghan D, Whiteley J. Cardiac electromechanics: the effect of contraction model on the mathematical problem and accuracy of the numerical scheme. *Q J Mech Appl Math*. 2010;63(3):375-399. doi:10.1093/qjmam/hbq014

96. Smith N, Nickerson D, Crampin E, Hunter P. Multiscale computational modelling of the heart. *Acta Numer*. 2004;13:371-431. doi:10.1017/S0962492904000200

97. Guccione JM, McCulloch AD. *Finite Element Modeling of Ventricular Mechanics*. Springer; 1991:121-144.

98. Zygote Media Group Inc. Zygote solid 3D heart generation II developement report. Technical Report. 2014.

99. Donea J, Giuliani S, Halleux JP. An arbitrary Lagrangian-Eulerian finite element method for transient dynamic fluidstructure interactions. *Comput Methods Appl Mech Eng*. 1982;33(1–3):689-723. doi:10.1016/0045-7825(82)90128-1

100. Hughes TJR, Liu WK, Zimmermann TK. Lagrangian-Eulerian finite element formulation for incompressible viscous flows. *Comput Methods Appl Mech Eng*. 1981;29(3):329-349. doi:10.1016/0045-7825(81)90049-9

101. Stein K, Tezduyar T, Benney R. Mesh moving techniques for fluid-structure interactions with large displacements. *J Appl Mech*. 2003; 70(1):58-63. doi:10.1115/1.1530635

102. Alharbi Y, Al Abed A, Bakir AA, et al. Fluid structure computational model of simulating mitral valve motion in a contracting left ventricle. *Comput Biol Med*. 2022;148:105834.

103. Hoffman J, Jansson J, Stöckli M. Unified continuum modeling of fluid-structure interaction. *Math Models Methods Appl Sci*. 2011;21(3): 491-513. doi:10.1142/S021820251100512X

104. Spühler JH, Hoffman J. An interface-tracking unified continuum model for fluid-structure interaction with topology change and full-friction contact with application to aortic valves. *Int J Numer Methods Eng*. 2021;122(19):5258-5278. doi:10.1002/nme.6384

105. Johnson AA, Tezduyar TE. Mesh update strategies in parallel finite element computations of flow problems with moving boundaries and interfaces. *Comput Methods Appl Mech Eng*. 1994;119(1–2):73-94. doi:10.1016/0045-7825(94)00077-8

106. Jasak H, Tukovic Z. Automatic mesh motion for the unstructured finite volume method. *Trans FAMENA*. 2006;30(2):1-20.

107. Corti M, Zingaro A, Quarteroni AM, et al. Impact of atrial fibrillation on left atrium haemodynamics: a computational fluid dynamics study. *Comput Biol Med*. 2022;150:106143. doi:10.1016/j.compbiomed.2022.106143

108. Fedele M, Faggiano E, Dede' L, Quarteroni A. A patient-specific aortic valve model based on moving resistive immersed implicit surfaces. *Biomech Model Mechanobiol*. 2017;16(5):1779-1803. doi:10.1007/s10237-017-0919-1

109. Fumagalli I, Fedele M, Vergara C, et al. An image-based computational hemodynamics study of the systolic anterior motion of the mitral valve. *Comput Biol Med*. 2020;123:103922. doi:10.1016/j.compbiomed.2020.103922

110. Fumagalli I, Vitullo P, Vergara C, et al. Image-based computational hemodynamics analysis of systolic obstruction in hypertrophic cardiomyopathy. *Front Physiol*. 2022;12:2437. doi:10.3389/fphys.2021.787082

111. Fumagalli I. A reduced 3D-0D FSI model of the aortic valve including leaflets curvature. *arXiv preprint arXiv:2106.00571* 2021. doi: 10.48550/arXiv.2106.00571

112. Astorino M, Gerbeau JF, Pantz O, Traoré KF. Fluid–structure interaction and multi-body contact: application to aortic valves. *Comput Methods Appl Mech Eng*. 2009;198(45–46):3603-3612. doi:10.1016/j.cma.2008.09.012

113. Dabiri Y, Yao J, Sack KL, Kassab GS, Guccione JM. Tricuspid valve regurgitation decreases after mitraclip implantation: fluid structure interaction simulation. *Mech Res Commun*. 2019;97:96-100. doi:10.1016/j.mechrescom.2019.04.009

114. Hsu MC, Kamensky D, Bazilevs Y, Sacks MS, Hughes TJ. Fluid–structure interaction analysis of bioprosthetic heart valves: significance of arterial wall deformation. *Comput Mech*. 2014;54(4):1055-1071. doi:10.1007/s00466-014-1059-4

115. Luraghi G, Wu W, De Gaetano F, et al. Evaluation of an aortic valve prosthesis: fluid-structure interaction or structural simulation? *J Biomech*. 2017;58:45-51. doi:10.1016/j.jbiomech.2017.04.004

116. Spühler JH, Jansson J, Jansson N, Hoffman J. 3D fluid-structure interaction simulation of aortic valves using a unified continuum ALE FEM model. *Front Physiol*. 2018;9:363. doi:10.3389/fphys.2018.00363

117. Terahara T, Takizawa K, Tezduyar TE, Bazilevs Y, Hsu MC. Heart valve isogeometric sequentially-coupled FSI analysis with the space–time topology change method. *Comput Mech*. 2020;65:1167-1187. doi:10.1007/s00466-019-01813-0

118. Bluestein D, Einav S. Transition to turbulence in pulsatile flow through heart valves – a modified stability approach. *J Biomech Eng*. 1994;116(4):477-487. doi:10.1115/1.2895799

119. Verkaik AC, Bogaerds ACB, Storti F, Van DeVosse F. A coupled overlapping domain method for the computation of transitional flow through artificial heart valves. Proceedings of the ASME Summer Bioengineering Conference. *Am Soc Mech Eng*. 2012;217-218.

120. Vignon-Clementel IE, Figueroa C, Jansen K, Taylor C. Outflow boundary conditions for 3D simulations of non-periodic blood flow and pressure fields in deformable arteries. *Comput Methods Biomech Biomed Engin*. 2010;13(5):625-640. doi:10.1080/10255840903413565

121. Bazilevs Y, Calo V, Cottrell J, Hughes T, Reali A, Scovazzi G. Variational multiscale residual-based turbulence modeling for large eddy simulation of incompressible flows. *Comput Methods Appl Mech Eng*. 2007;197(1–4):173-201. doi:10.1016/j.cma.2007.07.016

122. Bertoglio C, Caiazzo A. A tangential regularization method for backflow stabilization in hemodynamics. *J Comput Phys*. 2014;261:162-171. doi:10.1016/j.jcp.2013.12.057

123. Esmaily M, Bazilevs Y, Hsia TY, Vignon-Clementel IE, Marsden AL. A comparison of outlet boundary treatments for prevention of backflowdivergence with relevance to blood flowsimulations. *Comput Mech*. 2011;48(3):277-291. doi:10.1007/s00466-011-0599-0

124. Bazilevs Y, Takizawa K, Tezduyar TE. *Computational Fluid-Structure Interaction: Methods and Applications*. John Wiley & Sons; 2013.

125. Blanco PJ, Feijóo RA. A 3D-1D-0D computational model for the entire cardiovascular system. *Mec Comput*. 2010;29(59):5887-5911.

126. Quarteroni A, Veneziani A, Vergara C. Geometric multiscale modeling of the cardiovascular system, between theory and practice. *Comput Methods Appl Mech Eng*. 2016;302:193-252. doi:10.1016/j.cma.2016.01.007

127. Janela J, Moura dAB, Sequeira A. Comparing absorbing boundary conditions for a 3D non Newtonian fluid-structure interaction model for blood flow in arteries. *Mec Comput*. 2010;29(59):5961-5971.

128. Regazzoni F. Mathematical Modeling and Machine Learning for the Numerical Simulation of Cardiac Electromechanics. PhD thesis. Politecnico di Milano, Milano, Italy; 2020.

129. Krishnamoorthi S, Sarkar M, Klug WS. Numerical quadrature and operator splitting in finite element methods for cardiac electrophysiology. *Int J Numer Methods Biomed Eng*. 2013;29(11):1243-1266. doi:10.1002/cnm.2573

130. Pathmanathan P, Mirams GR, Southern J, Whiteley JP. The significant effect of the choice of ionic current integration method in cardiac electro-physiological simulations. *Int J Numer Methods Biomed Eng*. 2011;27(11):1751-1770. doi:10.1002/cnm.1438

131. Africa PC, Salvador M, Gervasio P, Dede L, Quarteroni A. A matrix-free high-order solver for the numerical solution of cardiac electrophysiology. *arXiv Preprint arXiv:2205.05136* 2022. doi: 10.48550/arXiv.2205.05136

132. Saad Y. Iterative Methods for Sparse Linear Systems. *SIAM*; 2003.

133. Xu J, Zikatanov L. Algebraic multigrid methods. *Acta Numer*. 2017;26:591-721. doi:10.1017/S0962492917000083

134. Salvador M, Dede' L, Quarteroni A. An intergrid transfer operator using radial basis functions with application to cardiac electromechanics. *Comput Mech*. 2020;66:491-511. doi:10.1007/s00466-020-01861-x

135. Fedele M, Quarteroni A. Polygonal surface processing and mesh generation tools for the numerical simulation of the cardiac function. *Int J Numer Methods Biomed Eng*. 2021;37(4):e3435. doi:10.1002/cnm.3435

136. VMTK. Accessed October 4, 2022, http://www.vmtk.org/. code repository: https://github.com/marco-fedele/vmtk.

137. Arndt D, Bangerth W, Blais B, et al. The deal.II library, version 9.2. *J Numer Math*. 2020;28(3):131-146. doi:10.1515/jnma-2020-0043

138. Arndt D, Bangerth W, Davydov D, et al. The deal.II finite element library: design, features, and insights. *Comput Math Appl*. 2021;81:407-422. doi:10.1016/j.camwa.2020.02.022

139. Official deal.ii. Accessed: October 4, 2022. https://www.dealii.org/.

140. Maceira AM, Prasad SK, Khan M, Pennell DJ. Normalized left ventricular systolic and diastolic function by steady state free precession cardiovascular magnetic resonance. *J Cardiovasc Magn Reson*. 2006;8(3):417-426. doi:10.1080/10976640600572889

141. Clay S, Alfakih K, Radjenovic A, Jones T, Ridgway JP. Normal range of human left ventricular volumes and mass using steady state free precession MRI in the radial long axis orientation. *MAGMA*. 2006;19(1):41-45. doi:10.1007/s10334-005-0025-8

142. Sugimoto T, Dulgheru R, Bernard A, et al. Echocardiographic reference ranges for normal left ventricular 2D strain: results from the EACVI NORRE study. *Eur Heart J Cardiovasc Imaging*. 2017;18(8):833-840. doi:10.1093/ehjci/jex140

143. Hammermeister K, Brooks R, Warbasse J. The rate of change of left ventricular volume in man: I. validation and peak systolic ejection rate in health and disease. *Circulation*. 1974;49(4):729-738. doi:10.1161/01.CIR.49.4.729

144. Fabian J, Epstein E, Coulshed N. Duration of phases of left ventricular systole using indirect methods. I. Normal subjects. *Br Heart J*. 1972;34(9):874-881. doi:10.1136/hrt.34.9.874

145. Benchimol A, Ellis JG. A study of the period of isovolumic relaxation in normal subjects and in patients with heart disease. *Am J Cardiol*. 1967;19(2):196-206. doi:10.1016/0002-9149(67)90533-4

146. LittleWC DTR. Clinical evaluation of left ventricular diastolic performance. *Prog Cardiovasc Dis*. 1990;32(4):273-290. doi:10.1016/0033-0620(90)90017-V

147. Emilsson K, Egerlid R, Nygren BM, Wandt B. Mitral annulus motion versus long-axis fractional shortening. *Exp Clin Cardiol*. 2006; 11(4):302.

148. Hawthorne EW. Dynamic geometry of the left ventricle. *Am J Cardiol*. 1966;18(4):566-573. doi:10.1016/0002-9149(66)90012-9

149. Feher JJ. *Quantitative Human Physiology: An Introduction*. Academic Press; 2017.

150. Gulsin G, Singh A, McCann GP. Cardiovascular magnetic resonance in the evaluation of heart valve disease. *BMC Med Imaging*. 2017; 17(1):1-14. doi:10.1186/s12880-017-0238-0

151. Kumar V, Abbas AK, Fausto N, Aster JC. *Robbins and Cotran Pathologic Basis of Disease, Professional Edition e-book*. Elsevier Health Science; 2014.

152. Stanfield CL. *Principles of Human Physiology*. Pearson; 2016.

153. Mark JB. *Atlas of Cardiovascular Monitoring*. Churchill Livingstone; 1998.

154. Murgo JP, Westerhof N, Giolma JP, Altobelli SA. Aortic input impedance in normal man: relationship to pressure wave forms. *Circulation*. 1980;62(1):105-116. doi:10.1161/01.CIR.62.1.105

155. Dusch MN, Thadani SR, Dhillon GS, Hope MD. Diastolic function assessed by cardiac MRI using longitudinal left ventricular fractional shortening. *Clin Imaging*. 2014;38(5):666-668. doi:10.1016/j.clinimag.2014.06.002

156. Pandian NG, Skorton DJ, Collins SM, Falsetti HL, Burke ER, Kerber RE. Heterogeneity of left ventricular segmental wall thickening and excursion in 2-dimensional echocardiograms of normal human subjects. *Am J Cardiol*. 1983;51(10):1667-1673. doi:10.1016/0002-9149(83)90207-2

157. Di Labbio G, Kadem L. Jet collisions and vortex reversal in the human left ventricle. *J Biomech*. 2018;78:155-160. doi:10.1016/j.jbiomech.2018.07.023

158. Pedrizzetti G, La Canna G, Alfieri O, Tonti G. The vortex—an early predictor of cardiovascular outcome? *Nat Rev Cardiol*. 2014;11(9): 545-553. doi:10.1038/nrcardio.2014.75

159. Lee AW, Nguyen UC, Razeghi O, et al. A rule-based method for predicting the electrical activation of the heart with cardiac resynchronization therapy from non-invasive clinical data. *Med Image Anal*. 2019;57:197-213. doi:10.1016/j.media.2019.06.017

160. Ma X, Gao H, Griffith BE, Berry C, Luo X. Image-based fluid–structure interaction model of the human mitral valve. *Comput Fluids*. 2013;71:417-425. doi:10.1016/j.compfluid.2012.10.025

161. Jhun CS, Newswanger R, Cysyk JP, et al. Dynamics of blood flows in aortic stenosis: mild, moderate, and severe. *ASAIO J*. 2021;67(6): 666-674. doi:10.1097/MAT.0000000000001296

162. Wood P. Aortic stenosis. *Am J Cardiol*. 1958;1(5):553-571. doi:10.1016/0002-9149(58)90138-3

163. Sahasakul Y, Edwards WD, Naessens JM, Tajik AJ. Age-related changes in aortic and mitral valve thickness: implications for two-dimensional echocardiography based on an autopsy study of 200 normal human hearts. *Am J Cardiol*. 1988;62(7):424-430. doi:10.1016/0002-9149(88)90971-X

APPENDIX A

A.1 | Solid mechanics constitutive laws

The Guccione strain energy is computed from the displacement $\mathbf{d}$ as[97]

$$\mathcal{W}_{\mathrm{G}}(\mathbf{d}) = \frac{c}{2}(\exp(Q) - 1) + \frac{\kappa}{2}(J - 1)\log(J),$$

where

$$Q = \sum_{i,j \in \{f,\, s,\, n\}} a_{i,j}(E\mathbf{j} \times \mathbf{i})^2 \ ,$$

$$E = \frac{1}{2}(F^T F - I) \ .$$

The strain energy function associated to the neo-Hookean model is given by[92]

$$\mathcal{W}_{\mathrm{NH}}(\mathbf{d}) = \frac{\mu}{2}\left(J^{-\frac{2}{3}} F : F - 3\right) + \frac{\kappa}{4}\left((J - 1)^2 + \log^2(J)\right) \ .$$

The values of the constant parameters appearing in both constitutive laws are reported in Appendix D.

APPENDIX B

B.1 | Valve modeling

The heart model includes the mitral valve in open configuration $\Gamma_{\mathrm{MV}}^{\mathrm{open}}$ and the aortic valve in closed configuration $\Gamma_{\mathrm{AV}}^{\mathrm{closed}}$. The opposite configurations, $\Gamma_{\mathrm{MV}}^{\mathrm{closed}}$ and $\Gamma_{\mathrm{AV}}^{\mathrm{open}}$, are obtained in a preprocessing step as described in Reference [43]. The procedure also yields the displacement vectors between the two configurations, that is two fields $\mathbf{d}_{\mathrm{k}} : \Gamma_{\mathrm{k}}^{\mathrm{closed}} \to \mathbb{R}^3$ such that

$$\Gamma_{\mathrm{k}}^{\mathrm{open}} = \left\{\mathbf{x}^{\mathrm{open}} \in \Omega_{\mathrm{f}} : \mathbf{x}^{\mathrm{open}} = \mathbf{x}^{\mathrm{closed}} + \mathbf{d}_{\mathrm{k}}(\mathbf{x}^{\mathrm{closed}}), \ \mathbf{x}^{\mathrm{closed}} \in \Gamma_{\mathrm{k}}^{\mathrm{closed}}\right\} \ .$$

Then, at any time $t \in (0, T)$ the configuration Γ_{k}^t of the valve is given by

$$\Gamma_{\mathrm{k}}^t = \left\{\mathbf{x}^t = \mathbf{x}^{\mathrm{closed}} + c_{\mathrm{k}}(t)\mathbf{d}_{\mathrm{k}}(\mathbf{x}^{\mathrm{closed}}) + \mathbf{d}_{\mathrm{ALE}}(\mathbf{x}^{\mathrm{closed}}, t), \ \mathbf{x}^{\mathrm{closed}} \in \Gamma_{\mathrm{k}}^{\mathrm{closed}}\right\} \ ,$$

wherein $c_{\mathrm{k}}(t)$ is a time-dependent opening coefficient that is equal to 0 when the valve is fully closed and to 1 when it is fully open. The functions $c_{\mathrm{k}}(t)$ are prescribed a priori, in the form

$$c_{\mathrm{k}}(t) = \begin{cases} 0 & \text{if } t \leq t_{\mathrm{k}}^{\mathrm{open}} \ , \\ \frac{1}{2}\left(1 - \cos\left(\pi \frac{1 - \exp\left\{-\chi_{\mathrm{k}}\left(t - t_{\mathrm{k}}^{\mathrm{open}}\right)/\Delta t_{\mathrm{k}}^{\mathrm{open}}\right\}}{1 - \exp(-\chi_{\mathrm{k}})}\right)\right) & \text{if } t_{\mathrm{k}}^{\mathrm{open}} < t \leq t_{\mathrm{k}}^{\mathrm{open}} + \Delta t_{\mathrm{k}}^{\mathrm{open}} \ , \\ 1 & \text{if } t_{\mathrm{k}}^{\mathrm{open}} + \Delta t_{\mathrm{k}}^{\mathrm{open}} < t < t_{\mathrm{k}}^{\mathrm{close}} \ , \\ 1 - \frac{1}{2}\left(1 - \cos\left(\pi \frac{1 - \exp\left\{-\chi_{\mathrm{k}}\left(t - t_{\mathrm{k}}^{\mathrm{close}}\right)/\Delta t_{\mathrm{k}}^{\mathrm{close}}\right\}}{1 - \exp(-\chi_{\mathrm{k}})}\right)\right) & \text{if } t_{\mathrm{k}}^{\mathrm{close}} < t \leq t_{\mathrm{k}}^{\mathrm{close}} + \Delta t_{\mathrm{k}}^{\mathrm{close}} \ , \\ 0 & \text{if } t > t_{\mathrm{k}}^{\mathrm{close}} + \Delta t_{\mathrm{k}}^{\mathrm{close}} \ . \end{cases}$$

The parameters p_{k}, $\Delta t_{\mathrm{k}}^{\mathrm{open}}$ and $\Delta t_{\mathrm{k}}^{\mathrm{close}}$ are prescribed and they determine the opening speed of the valve. The opening time $t_{\mathrm{k}}^{\mathrm{open}}$ is the first instant at which the difference between upstream and downstream pressures is positive, while the

closing time t_k^{close} is the first instant at which the pressure difference is negative. Pressure difference is evaluated averaging over spherical control volumes as in Reference [43] (Figure 5C).

We remark that we displace the valves following the fluid domain. Moreover, we take $\mathbf{u}_{\Gamma_k} = \mathbf{0}$ that is, we neglect the valve velocity due to the change of its configuration. This corresponds to a quasi-static approximation of the valve opening and closing.[108]

APPENDIX C

C.1 | Blood circulation model

The equations for the blood circulation model read: for $t \in (0, T)$,

$$
\begin{cases}
C_{AR}^{SYS} \dfrac{dp_{AR}^{SYS}(t)}{dt} = Q_{AV}(t) - Q_{AR}^{SYS}(t), \\[2mm]
\dfrac{L_{AR}^{SYS}}{R_{AR}^{SYS}} \dfrac{dQ_{AR}^{SYS}(t)}{dt} = -Q_{AR}^{SYS}(t) - \dfrac{p_{VEN}^{SYS}(t) - p_{AR}^{SYS}(t)}{R_{AR}^{SYS}}, \\[2mm]
C_{VEN}^{SYS} \dfrac{dp_{VEN}^{SYS}(t)}{dt} = Q_{AR}^{SYS}(t) - Q_{VEN}^{SYS}(t), \\[2mm]
\dfrac{L_{VEN}^{SYS}}{R_{VEN}^{SYS}} \dfrac{dQ_{VEN}^{SYS}(t)}{dt} = -Q_{VEN}^{SYS}(t) - \dfrac{p_{RA}(t) - p_{VEN}^{SYS}(t)}{R_{AR}^{SYS}}, \\[2mm]
p_{RA}(t) = p_{EX}(t) + E_{RA}(t)(V_{RA}(t) - V_{0,RA}), \\[2mm]
\dfrac{dV_{RA}(t)}{dt} = Q_{VEN}^{SYS}(t) - Q_{TV}(t), \\[2mm]
Q_{TV}(t) = \dfrac{p_{RA}(t) - p_{RV}(t)}{R_{TV}(p_{RA}(t),\ p_{RV}(t))}, \\[2mm]
p_{RV}(t) = p_{EX}(t) + E_{RV}(t)(V_{RV}(t) - V_{0,RV}), \\[2mm]
\dfrac{dV_{RV}(t)}{dt} = Q_{TV}(t) - Q_{PV}(t), \\[2mm]
Q_{PV}(t) = \dfrac{p_{RV}(t) - p_{AR}^{PUL}(t)}{R_{PV}(p_{RV}(t),\ p_{AR}^{PUL}(t))}, \\[2mm]
C_{AR}^{PUL} \dfrac{dp_{AR}^{PUL}(t)}{dt} = Q_{PV}(t) - Q_{AR}^{PUL}(t), \\[2mm]
\dfrac{L_{AR}^{PUL}}{R_{AR}^{PUL}} \dfrac{dQ_{AR}^{PUL}(t)}{dt} = -Q_{AR}^{PUL}(t) - \dfrac{p_{VEN}^{PUL}(t) - p_{AR}^{PUL}(t)}{R_{AR}^{PUL}}, \\[2mm]
C_{VEN}^{PUL} \dfrac{dp_{VEN}^{PUL}(t)}{dt} = Q_{AR}^{PUL}(t) - Q_{VEN}^{PUL}(t), \\[2mm]
p_{LA}^{in}(t) = p_{VEN}^{PUL}(t) - R_{VEN}^{PUL} Q_{VEN}^{PUL}(t) - L \dfrac{dQ_{VEN}^{PUL}(t)}{dt},
\end{cases}
\tag{C1}
$$

endowed with suitable initial conditions. In the above system, $p_{EX}(t) = 0$ represents an external pressure, $E_{RA}(t)$ and $E_{RV}(t)$ are time-varying elastances modeling the contraction of the right atrium and ventricle, defined as

$$
E_i(t) = E_i^B + E_i^B \varphi_{act}(t, t_c^i, T_c^i, T_r^i),
$$

φ_{act} is defined as in Reference [30], and $V_{0,RA}$ and $V_{0,RV}$ are the resting volumes of left atrium and ventricle. Valvular resistances R_{TV} and R_{PV} are given by

$$
R_k(p_1, p_2) = \begin{cases} R_{max} & \text{if } p_1 < p_2, \\ R_{min} & \text{if } p_1 \geq p_2, \end{cases} \quad k \in \{TV, PV\}.
$$

The rest of the resistances, capacitances and inductances are parameters surrogating the properties of the circulation network.

APPENDIX D

D.1 | Derivation of the flowrate fluid-circulation coupling condition

We aim at coupling the 3D fluid model and the 0D circulation model in such a way that the volume of blood entering (exiting) the 3D domain is balanced by an equivalent flow rate exiting (entering) the 0D model. Let us consider, for simplicity of derivation, a situation in which the 3D model has only one open boundary, $\Gamma^{\text{out}} \subset \partial\Omega_{\text{f}}$, while the rest of the boundary is formed by the fluid–solid interface Σ. We assume that the 3D and 0D models are coupled through Γ^{out}, and denote by Q the flowrate incoming in the 0D model at the 3D-0D interface.

Denoting by $V_{3D}(t)$ the volume of the 3D fluid domain Ω_{f}, by Reynolds' transport theorem there holds:

$$\frac{dV_{3D}}{dt} = \frac{d}{dt}\int_{\Omega_{\text{f}}} 1 d\mathbf{x} = \int_{\partial\Omega_{\text{f}}} \mathbf{u}_{\text{ALE}} \times \mathbf{n} d\sigma = \int_{\partial\Omega_{\text{f}}} \mathbf{u} \times \mathbf{n} d\sigma + \int_{\partial\Omega_{\text{f}}} (\mathbf{u}_{\text{ALE}} - \mathbf{u}) \times \mathbf{n} d\sigma .$$

By the incompressibility constraint, the first term on the right-hand side of the previous equation vanishes, so that

$$\frac{dV_{3D}}{dt} = \int_{\partial\Omega_{\text{f}}} (\mathbf{u}_{\text{ALE}} - \mathbf{u}) \times \mathbf{n} d\sigma = \int_{\Sigma} (\mathbf{u}_{\text{ALE}} - \mathbf{u}) \times \mathbf{n} d\sigma + \int_{\Gamma^{\text{out}}} (\mathbf{u}_{\text{ALE}} - \mathbf{u}) \times \mathbf{n} d\sigma .$$

On Σ, we impose the no-slip condition $\mathbf{u} = \mathbf{u}_{\text{ALE}}$, so that the previous equation rewrites as

$$\frac{dV_{3D}}{dt} = \int_{\Gamma^{\text{out}}} (\mathbf{u}_{\text{ALE}} - \mathbf{u}) \times \mathbf{n} d\sigma .$$

The quantity $\frac{dV}{dt}$ expresses the amount of blood incoming through Γ^{out}, which, up to a change in sign, must equal the flow rate entering the first compartment of the 0D circulation model. The resulting coupling condition reads:

$$Q = \int_{\Gamma^{\text{out}}} (\mathbf{u} - \mathbf{u}_{\text{ALE}}) \times \mathbf{n} d\sigma .$$

This derivation can be generalized to the case of multiple inflow and outflow boundaries.

APPENDIX E

E.1 | Model parameters

We report a list of the parameters used for the simulation described in Section 3. Table D1 reports parameters for the electrophysiology model, Table D2 those for the force generation model, Table D3 those for the solid mechanics model, Table D4 lists the parameters used in the fluid dynamics model and Tables D5 and D6 those of the circulation model. For the RDQ20-MF force generation model, we only report those parameters whose values differ from those presented in Reference [66]. We refer the interested reader to Reference [83] for details on the parameters of the TTP06 ionic model.

TABLE D1 Parameters used in the electrophysiology model

	Parameter	Value	
Monodomain	χ	1400	1 cm
	C_m	1	F cm^2
Conductivities	$\sigma_m^l/(\chi C_m)$	2.00×10^{-4}	m^2/s
	$\sigma_m^t/(\chi C_m)$	1.05×10^{-4}	m^2/s
	$\sigma_m^n/(\chi C_m)$	0.55×10^{-4}	m^2/s
Stimulus	A_{app}/C_m	25.71	V/s
	σ_{app}	2.5×10^{-3}	m
	T_{app}	3	ms

Note: Conductivities were tuned to obtain a conduction velocity of 0.6 m/s, 0.4 m/s and 0.2 m/s along fibers, sheets and normal-to-fiber directions, respectively. The parameters used for the ionic model are those of the original paper.[83]

TABLE D2 Parameters used in the force generation model

Parameter	Value	
γ	30	
k_d	0.36	
α_{k_d}	-0.2083	
K_{off}	8	1/s
K_{basic}	4	1/s
μ_{fp}^0	32.255	1/s
μ_{fp}^1	0.768	1/s
a_{XB}	8.9491×10^8	Pa
SL_0	2.1	m

Note: We only report those parameters whose values differ from the original setting described in Reference [66].

TABLE D3 Parameters used in the solid mechanics model

	Parameter	Value	
	ρ_s	1000	kg/m^2
Guccione (atrium and ventricle)	c	8.8×10^2	Pa
	a_{ff}	8	
	a_{ss}	6	
	a_{nn}	3	
	a_{fs}	12	
	a_{fn}	3	
	a_{sn}	3	
	κ	5×10^4	Pa
Atrioventricular ring	μ	5×10^6	Pa
	κ	1×10^6	Pa
Ascending aorta	μ	5.25×10^5	Pa
	κ	1×10^6	Pa
Boundary conditions	$K_\perp^{epi}$	2×10^5	Pa/m
	$K_\parallel^{epi}$	2×10^4	Pa/m
	$C_\perp^{epi}$	2×10^4	Pa s/m
	$C_\parallel^{epi}$	2×10^3	Pa s/m
Initial conditions	p_0^{LA}	9.75	mmHg
	p_0^{ring}	11.25	mmHg
	p_0^{LV}	11.25	mmHg
	p_0^{AA}	80	mmHg
Interface regularization	ψ_{th}^{LV}	0.2	
	ψ_{th}^{LA}	0.1	

TABLE D4 Parameters used in the fluid dynamics model

	Parameter	Value	
Navier–Stokes	ρ_f	1060	kg/m^3
	μ_f	3.5×10^{-3}	Pa s
Valve modeling	R_{MV}, R_{AV}	1×10^5	kg/m s
	$\varepsilon_{MV}, \varepsilon_{AV}$	0.75×10^{-3}	m
	Δt_{MV}^{open}	10	ms
	Δt_{AV}^{open}	10	ms
	Δt_{MV}^{close}	30	ms
	Δt_{AV}^{close}	80	ms
	χ_{MV}, χ_{AV}	-3	

Note: Valve half-thicknesses ε_{MV} and ε_{AV} were chosen to match literature data.[45,163] Resistances R_{MV}, R_{AV} were chosen to be sufficiently high to guarantee minimal spurious flow through valves without hindering the conditioning of the FSI system.

TABLE D5 Parameters used in the circulation model: systemic and pulmonary circulation

	Parameter	Value	
Systemic arteries	R_{AR}^{SYS}	0.45	mmHg s/ml
	C_{AR}^{SYS}	2.19	ml/mmHg
	L_{AR}^{SYS}	2.7×10^{-3}	mmHg s^2/ml
	$R_{upstream}^{SYS}$	0.07	mmHg s/ml
	$p_{AR}^{SYS}(0)$	80	mmHg
	$Q_{AR}^{SYS}(0)$	66.5775	ml/s
Systemic veins	R_{VEN}^{SYS}	0.26	mmHg s/ml
	C_{VEN}^{SYS}	60	ml/mmHg
	L_{VEN}^{SYS}	5×10^{-4}	mmHg s^2/ml
	$p_{VEN}^{SYS}(0)$	30.9029	mmHg
	$Q_{VEN}^{SYS}(0)$	89.6295	ml/s
Pulmonary arteries	R_{AR}^{PUL}	0.05	mmHg s/ml
	C_{AR}^{PUL}	10	ml/mmHg
	L_{AR}^{PUL}	5×10^{-4}	mmHg s^2/ml
	$p_{AR}^{PUL}(0)$	20.0	mmHg
	$Q_{AR}^{PUL}(0)$	69.3166	ml/s
Pulmonary veins	R_{VEN}^{PUL}	0.025	mmHg s/ml
	C_{VEN}^{PUL}	38.4	ml/mmHg
	L_{VEN}^{PUL}	2.083×10^{-4}	mmHg s^2/ml
	$p_{VEN}^{PUL}(0)$	17.0	mmHg
	$Q_{VEN}^{PUL}(0)$	105.523	ml/s

TABLE D6 Parameters used in the circulation model: right heart

	Parameter	Value	
Valves	R_{min}	7.5×10^{-3}	mmHg s/ml
	R_{max}	7.5×10^{4}	mmHg s/ml
Right atrium	E_A	0.06	mmHg/ml
	E_B	0.07	mmHg/ml
	t_C	0.8	
	T_C	0.17	
	T_R	0.17	
	$V_{0,RA}$	4	ml
	$V_{RA}(0)$	64.1702	ml
Right ventricle	E_A	0.55	mmHg/ml
	E_B	0.05	mmHg/ml
	t_C	0.0	
	T_C	0.34	
	T_R	0.15	
	$V_{0,RV}$	16	ml
	$V_{RV}(0)$	148.9384	ml